Design, characterization, and fabrication of solar-retroreflective cool-wall materials

Ronnen Levinson[1,*], Sharon Chen[1], Jonathan Slack[1], Howdy Goudey[1], Tatsuya Harima[2], and Paul Berdahl[1]

[1] Heat Island Group, Lawrence Berkeley National Laboratory, 1 Cyclotron Road, Berkeley, CA 94720, USA

[2] Electronic Components & Environment Solutions Business Unit, Dexerials Corporation, 1724 Shimotsuboyama, Shimotsuke-shi, Tochigi 323-0194, Japan

* Corresponding author. Email: RML27@cornell.edu; tel. +1-510-486-7494.

16 July 2019

Abstract

Raising urban albedo increases the fraction of incident sunlight returned to outer space, cooling cities and their buildings. We evaluated the angular distribution of solar radiation incident on exterior walls in 17 U.S. climates to develop performance parameters for solar-retroreflective walls, then applied first-principle physics and ray-tracing simulations to explore designs. Our analysis indicates that retroreflective walls must function at large incidence angles to reflect a substantial portion of summer sunlight, and that this will be difficult to attain with materials that rely on total internal reflection.

Gonio-spectrophotometer measurements of the solar spectral bi-directional reflectivity of a bicycle reflector showed little to no retroreflection at large incidence angles. Visual comparison of retroreflection to specular first-surface reflection for four different retroreflective safety films using violet and green lasers suggest their retroreflection to be no greater than 0.09 at incidence angles up to 45°, and no greater than 0.30 at incidence angles of up to 70°.

Attempts to produce a two-surface retroreflector with orthogonal mirror grooves by cutting and polishing an aluminum block indicate that residual surface roughness impedes retroreflection. Ongoing efforts focus on forming orthogonal surfaces with aluminized Mylar film, a material with very high specular reflectance across the solar spectrum. We investigated (1) folding or stamping a free film; (2) adhering the film to a pre-shaped substrate; and (3) attaching the film to a flat ductile substrate, then shaping. The latter two methods were more successful but produced imperfect right angles.

Keywords

solar retroreflector; cool wall; goniometer; solar spectral bi-directional reflectance intensity; ray tracing; aluminized Mylar

1 Introduction

Raising urban albedo (solar reflectance) increases the fraction of incident sunlight returned to outer space, cooling cities and their buildings [1,2]. It can also reduce atmospheric temperature via negative radiative forcing, abating global warming [3–6]. “Cool” horizontal surfaces with high solar reflectance, such as white roofs and light-colored pavements, are ideal solutions for a low-density city with short buildings, in which most of the sunlight is intercepted by roofs and pavements [7–13]. However, in a densely populated urban area with many tall buildings, more sunlight may fall on walls than on roofs or pavements. Light diffusely reflected from a vertical surface can strike neighboring buildings, pavements, or pedestrians [14,15].

Figure 1 illustrates three idealized reflections: specular (perfectly mirrorlike), Lambertian (perfectly diffuse), and retro (back to source). We can increase the effective albedo of urban areas, and prevent heating of neighboring buildings, by making building walls retroreflective. The two-surface corner retroreflector shown in the Electronic Supplementary Material (ESM) as ESM Figure A-1a will return light to its source if incident in plane of page; the spherical retroreflector shown in ESM Figure A-1b and the three-surface corner retroreflector shown in ESM Figure A-2 will each return light incident from any direction to its source. Retroreflective cool walls could improve upon diffusely reflecting cool walls by reflecting incoming beam radiation to the solar disc (if the retroreflection is three dimensional and ideal) or at least upwards (if the retroreflection is two dimensional and/or imperfect). This can increase the fraction of sunlight reflected out of the urban canyon formed by the walls of neighboring buildings and the ground between them.

Today, corner and spherical retroreflectors are widely used for traffic safety, remote sensing, and optical communication. Here we explore the application of solar retroreflectors to exterior walls.

For example, consider an isolated building with 0.60 wall albedo and 0.20 ground albedo, each surface a Lambertian reflector. About 36% of the sunlight incident on the wall would return to the sky [0.60 wall albedo × (0.5 sky view factor + 0.5 ground view factor × 0.20 ground albedo)] (Figure 2a). If the wall were instead covered with a retroreflector of equal albedo—say, orthogonal mirror pairs, each surface of albedo 0.775, with a two-bounce albedo of $0.775^2 = 0.60$ (ESM Figure A-1a)—it would reflect upward 60% of incident beam sunlight, and about 30% of the incident diffuse sunlight (of the 60% of diffuse light that is reflected, half will go up, and half will go down). If 20% of the incident sunlight is diffuse, the final fraction returned to the sky would be 80% × 0.60 wall solar retroreflectance + 20% × [0.60 wall solar diffuse reflectance × (0.5 sky view factor + 0.5 ground view factor × 0.20 ground albedo)] = 55% (Figure 2b).

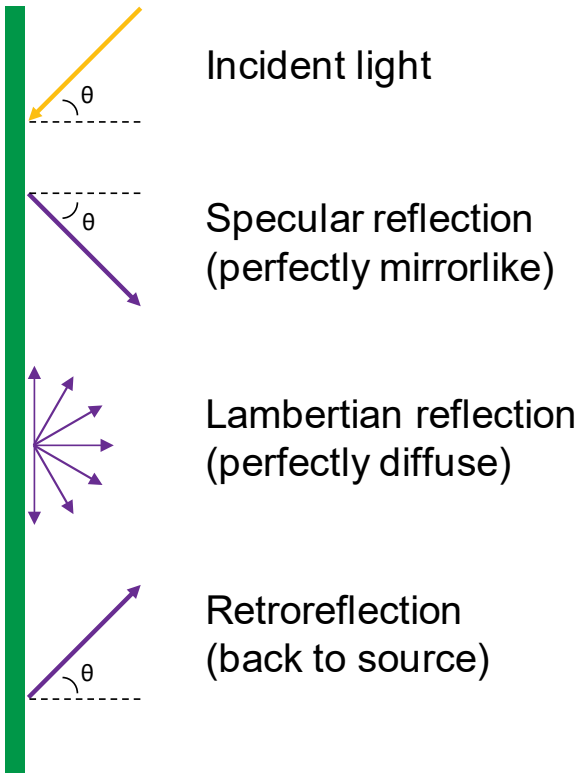

Figure 1. Specular, Lambertian, and retro reflection of beam light striking a vertical surface.

A Lambertian wall would have to reflect 92% of incident sunlight to return 55% of incident sunlight to the sky [0.92 wall albedo × (0.5 sky view factor + 0.5 ground view factor × 0.20 ground albedo)] (Figure 2c).

Introducing a neighboring building reduces wall and ground sky view factors, but does not impede retroreflection. Hence the boost in skyward reflection offered by substituting a retroreflective wall for a Lambertian wall will be even greater for a wall within the urban canyon.

The current study explores the design, characterization, and fabrication of solar-retroreflective wall materials. First, we review the state of the art of retroreflectance measurement and retroreflector technology. Second, we consider the design of wall solar retroreflectors, including performance requirements and the potential to meet these requirements with various materials and geometries. Third, we describe the instruments that we use to measure or visualize retroreflection. Fourth, we characterize the performance of some commercially available retroreflectors. Fifth, we fabricate and evaluate 2-D solar retroreflectors for walls.

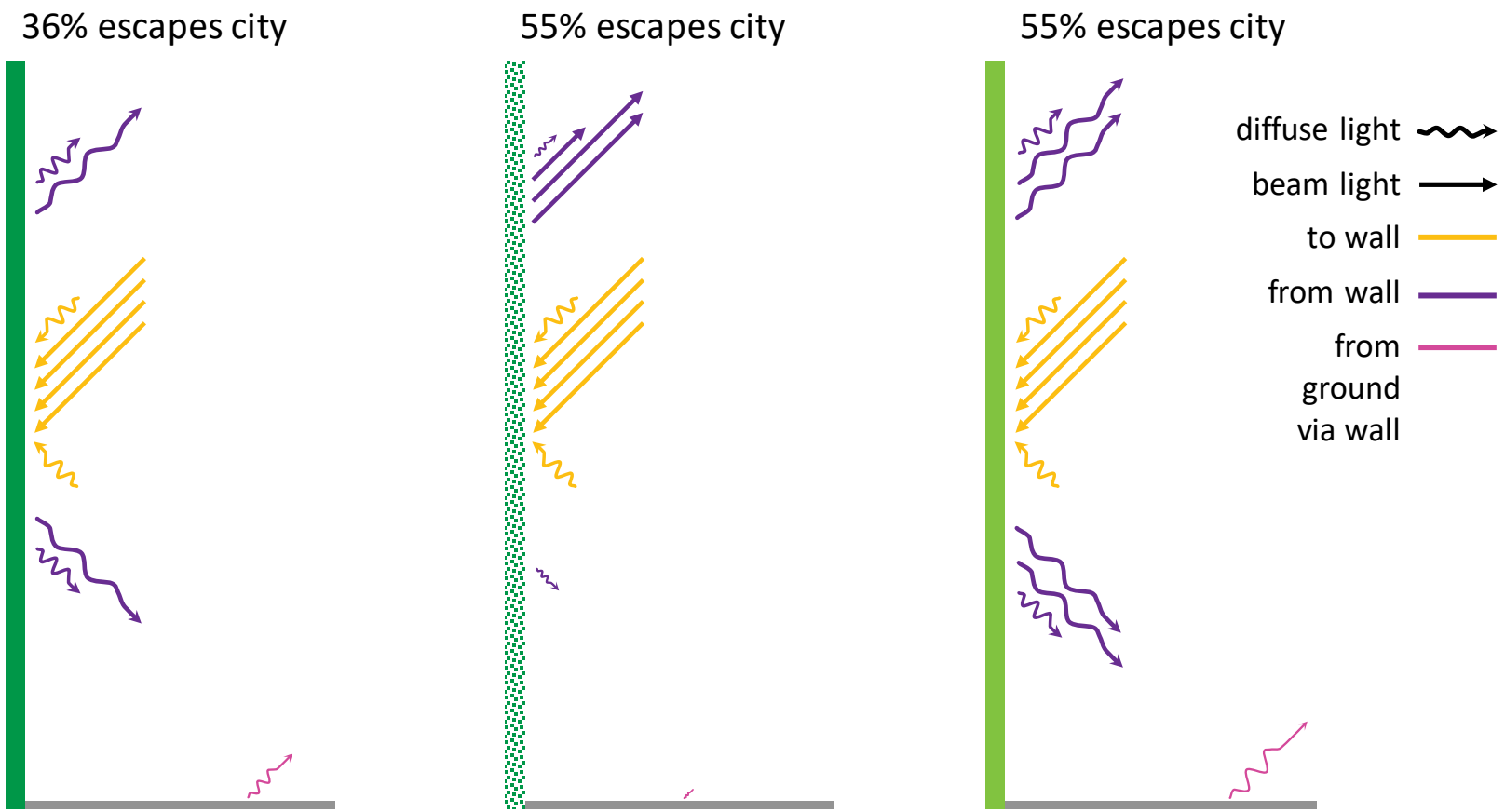

Figure 2. Retroreflective cool surfaces can help sunlight that strikes walls escape the city. The out-of-city reflection from a retroreflective isolated wall of albedo 0.60 (panel b) will be more than 50% greater than that from a Lambertian isolated wall of the same albedo (panel a), and will equal that from a Lambertian isolated wall of albedo 0.92 (panel c).

2 Literature review

2.1 Overview

Yuan et al. [16] comprehensively reviewed research on the application of retroreflective materials to the building envelope, including measurement of retroreflectance, ability to increase urban albedo, and potential energy savings; the only topic minimally addressed was materials development. Here we focus on past characterization, design, and fabrication of retroreflective cool surfaces for walls to identify strategies relevant to walls. We do not further discuss studies of the *benefits* of retroreflective wall materials, other than to note that such research published subsequent to (or simply not included in) the review by Yuan et al. [16] includes measurement of wall temperature reductions [17] and canyon albedo increases [18,19] in small-scale urban canyon models with retroreflective walls.

2.2 Measurement of retroreflectance

Retroreflectance can be assessed by (A) measuring retroreflection with coincident light source and light detector, such as those in a fiber spectrophotometer [20–22]; (B) measuring bi-directional reflectivity, or at least the angular distribution of reflected light, with a goniometer [23–31]; or (C) using calorimetry to gauge directional-hemispherical solar reflectance from temperature rise in the sun, then subtracting from this value directional-hemispherical solar reflectance measured in a spectrophotometer with fitted with an integrating sphere [32–35]. Method C works because perfectly retroreflected light escapes through the inlet port of the integrating sphere.

Method A and those implementations of Method B that do not measure specimen irradiance yield information about the distribution of reflected light, but not retroreflectance (fraction of incident radiation that is retroreflected). Method B can yield retroreflectance at arbitrary incidence angle if irradiance is measured at both specimen and observer. Method C directly yields solar retroreflectance, but only at near-normal incidence unless the spectrophotometer can measure directional-hemispherical reflectance at other incidence angles.

2.2.1 Method A (coincident source and detector)

Iyota et al. [20] and Yuan et al. [21,22] measured angular distribution of solar spectral reflection (400 – 1,715 nm) with a repositionable fiber-optic spectrophotometer. Yuan et al. [21,22] scaled near-normal solar retroreflectance obtained via Method C (calorimeter and spectrophotometer) by the ratio of reflection at far-from-normal incidence to that at near-normal incidence to estimate solar retroreflectance at far-from-normal incidence.

2.2.2 Method B (goniometer)

Rossi et al. [23] used a repositionable photodetector (nine observer angles ranging from -70° to 70°; broadband response 450 – 950 nm) to measure the angular distribution of light reflected from a specimen illuminated with a normally incident xenon-arc artificial solar light source. They reported irradiance at the

detector (power/area) as a function of observer angle. Rossi et al. [24] measured the angular distribution of reflected light using a semicircular array of 19 fixed photodiodes (observer angles -90° to 90°; broadband response 360-1,100 nm); illumination was provided by the same artificial solar light source used by Rossi et al. [23], but the detector array and the specimen platform (one unit) could be tilted to vary incidence angle. Morini et al. [29] modified the apparatus of Rossi et al. [24] by substituting a blue, green, or red laser for the artificial solar light source, and determined that the photodiode detectors responded best to the red laser. Castellani et al. [25] and Morini et al. [30] further simplified this apparatus by using only the red laser. Rossi et al. [24], Castellani et al. [25], and Morini et al. [29,30] reported the ratio of the signal from each detector to the sum of signals returned by all detectors.

Harima and Nagahama [26,27] and Ichinoise et al. [28] measured spectral bi-directional reflectivity with a two-axis solar gonio-spectrophotometer with three spectral photodetectors spanning 350 – 2,350 nm. The gonio-spectrophotometer could tilt the specimen 0 to 180°, and measure light reflected at any angle.

Mauri et al. [31] measured angular distribution of reflected light with a two-axis gonio-reflectometer (reflection angle -90° to 90°; broadband response 390 – 700 nm). Illumination was provided by a tungsten halogen lamp, and the specimen platform could be tilted to vary incidence angle.

2.2.3 Method C (calorimeter and spectrophotometer)

Sakai et al. [32] and Yuan et al. [33,34] estimated the solar reflectances of retroreflective test specimens by comparing their temperature rises under near-normal direct sunlight to those of non-retroreflective reference specimens, then subtracting near normal-hemispherical solar reflectance measured in a UV-vis-NIR spectrophotometer with integrating sphere. These studies used stationary specimens in their calorimetric trials.

Levinson et al. [35] estimated the effective solar reflectances of fluorescent test specimens by comparing their temperature rises in the sun to those of non-fluorescent reference specimens. Their apparatus rotated the specimens on a platter to minimize errors that result from variations in convection. This instrument can also be used to measure the solar reflectances of retroreflective test specimens by comparing their temperatures under the sun to those of non-retroreflective reference specimens.

2.3 Retroreflective materials

2.3.1 Retroreflective sheeting for traffic control

ASTM D4956-17: Standard Specification for Retroreflective Sheeting for Traffic Control [36] classifies traffic-control retroreflective sheeting materials according to composition and to performance requirements for minimum coefficient of reflection, outdoor weathering, and daytime luminance factor. Classes of commercial retroreflective sheeting materials evaluated for application to buildings or streets include enclosed (a.k.a. embedded) lens glass bead (ASTM D4956 Type 1, a.k.a. “engineering grade”; or Type 2, a.k.a. “super engineer grade”), encapsulated lens glass bead (Type 3, a.k.a. “high-intensity”), unmetallized microprism (also Type 3), and unmetallized cube corner microprism (Type 8 or Type 9; neither has a common name) [17–20,23,24,33,34,37].

Sakai et al. [32] applied Method C (calorimeter and spectrophotometer) to measure near-normal (7° incidence) solar retroreflectances of 0.049 – 0.129 for enclosed lens glass bead sheeting, 0.178 for an encapsulated lens glass bead sheet, and 0.235 – 0.295 for microprismatic sheeting. Yuan et al. [33] applied Method C to measure the near-normal (7° incidence) solar retroreflectances of a Type 3 encapsulated lens glass bead sheet (0.18 when new; 0.0072 after 25 months of natural exposure in Osaka, Japan) and a Type 9 microprismatic sheet (0.44 when new; 0.42 after 25 months). Yuan et al. [21] applied Method C to measure the near-normal solar retroreflectance of a Type 9 microprismatic sheet (0.41), then scaled this result by reflectance intensities measured with Method A (coincident source and detector, spectrum 400 – 1,715 nm) to estimate solar retroreflectance at incidence angles ranging up to 90°; retroreflectance was about 0.37 at 25° incidence, and declined sharply at larger incidence angles. Yuan et al. [22] repeated this process for a Type 3 encapsulated lens glass bead sheet, obtaining near-normal solar retroreflectance 0.18; retroreflectance was essentially unchanged at incidence 25° and 0.152 at incidence 45°, declining quickly thereafter.

Following Method B (goniometer) Rossi et al. [23] found that when illuminated at normal incidence, two enclosed lens glass beads sheets (Types 1 and 2), two encapsulated lens glass bead sheets (Types 2 and 3), and two unmetallized microprismatic sheets (Type 8) preferentially returned light at observer angles -10° to 10°, with peak signal at 0°. Rossi et al. [24] applied Method B to three enclosed lens glass bead sheets (Types 1 and 2) and two microprismatic sheets (Types 3 and 8). By measuring fractional distribution by observer angle (-90° to 90°) of reflected lamplight while varying incidence angle from 10° to 80°, they found that the enclosed lens glass bead sheets retroreflected light incident at up to 30° or 40°, while the microprismatic sheets retroreflected light incident at up to 30°. Absolute retroreflectance was not reported.

2.3.2 Other retroreflective technologies

Other retroreflective technologies explored for building or street application include a custom prismatic sheet [38], glass beads over paint [21,22,29,39,40], tiles coated with microspheres [25,30], a window film that selectively retroreflects near-infrared sunlight [26], and a granule-surfaced asphaltic (bituminous) roofing shingle [31].

Yuan et al. [38] created a custom prismatic sheet formed by surfacing the front of a Type 9 unmetallized cube corner prismatic sheet with clear glass and its back with white plastic. Measured following Method C (calorimeter and spectrophotometer), the near-normal (7° incidence) solar retroreflectance of this system was 0.44 when new, decreasing by only 0.02 after 485 days of natural exposure in Osaka.

Yuan et al. [21] applied Method C to measure the near-normal (7° incidence) solar retroreflectances of white paint surfaced with glass beads with real refractive index 1.5 or 1.9, obtaining 0.007 for the former and 0.062 for the latter. Scaling by reflectance intensities measured with Method A (coincident source and detector, spectrum 400 – 1,715 nm) indicated that solar retroreflectance would drop to half near-normal value at 25° incidence, then decline slowly through incidence angle 65°. Yuan et al. [22] repeated this process for eight specimens created by applying at two different coverage densities glass beads with real refractive index 1.5 or 1.9, over white paint or silver paint; results were similar to those for the bead-

over-paint systems characterized by Yuan et al. [21]. Yuan et al. [40] exposed four such bead-over-paint systems in Osaka, and found no significant loss of solar retroreflectance after one year.

Morini et al. [29] covered light-colored paint with either small glass spheres (diameter 0.1 – 0.2 mm) or large glass spheres (diameter 3 mm), and found via goniometer measurement (Method B) that these specimens retroreflected blue, green, and red laser beams incident at up to 60°.

Castellani et al. [25] used tape casting to surface grey and white ceramic tiles with a retroreflective paint prepared by suspending barium titanate glass microspheres in a clear resin. Spheres were uncoated, hemispherically undercoated with aluminum to enhance reflectance, or hemispherically undercoated with aluminum and then overcoated with a fluoropolymer that pushed the sphere to the resin-air interface. Following Method B (goniometer), they found that the painted tiles retroreflected red laser light incident at up to 60°; absolute retroreflectance was not reported. Spheres with aluminum undercoating substantially changed tile color.

In a similar study, Morini et al. [30] characterized light-brown ceramic tiles surfaced with a retroreflective paint prepared by suspending uncoated sodium tempered glass microspheres or uncoated barium titanate glass microspheres in a clear resin using the same apparatus employed by Castellini et al. [25]. Reflectance patterns for the sodium tempered glass microspheres and barium titanate glass microspheres were comparable to each other, and similar to those reported for uncoated titanium glass microspheres by Castellini et al. [25]. The global solar reflectance yielded by the sodium tempered glass microspheres was lower than produced by the barium titanate microspheres. Absolute solar retroreflectance was not reported.

Following Method B (goniometer), Harima and Nagahama [26] measured the solar spectral bi-directional reflectivity of a special solar-control window film designed to help mitigate the urban island effect by retroreflecting near-infrared sunlight while transmitting visible sunlight. The downward reflectance of solar radiation incident at a polar angle of 70° and an azimuth angle of 0° was about half that of a conventional solar control window film.

Mauri et al. [31] used Method B (goniometer) to characterize the directional reflectance of a granule-surfaced asphaltic roofing shingle. The shingle exhibited some retroflection when illuminated at incidence angles of 45° and 60°.

Sakai and Iyota [41] created a wall retroreflector designed to provide cooling in summer and heating in winter by retroreflecting sunlight when the sun is high (large incidence angle) and absorbing sunlight when the sun is low (small incident angle). A ball lens directed light incident at large angles to a mirror substrate and light incident at small angles to a black substrate. By comparing the temperature in the sun of this prototype to those of black and white reference surfaces, they found that the directional-hemispherical solar reflectance of their prototype was about 0.60 at incidence angles greater than 30°, and about 0.35 at incidence angles less than 30°. They did not report retroreflectance.

3 Design

3.1 Overview

A safety retroreflector makes a sign easier to read in low light (e.g., at night, or in a tunnel) by reflecting vehicle headlamp illumination to the driver. If the sign is far away, making the path from sign to driver nearly parallel to that from headlamp to sign, modest retroreflection of headlamp light arriving at near-normal incidence will suffice. Only visible light (400 – 700 nm) need be reflected [36].

To reduce the solar heat gain of the building and its surroundings, a *wall* retroreflector must reflect a large fraction of incident sunlight. Sunlight will strike the wall over a wide range of incidence angles, and about half the radiative energy in sunlight arrives in the invisible near-infrared spectrum (700 – 2,500 nm) [42]. Thus, the design requirements for a wall retroreflector differ significantly from those for a safety retroreflector.

3.2 Angular distribution of solar irradiation

To explore the distribution of angles at which beam sunlight strikes walls, we computed hourly solar positions and hourly beam tilt irradiances on isolated walls following the standard isotropic sky model [43]. We set ground albedo to 0.20, obtained global horizontal and diffuse horizontal hourly solar irradiation values from Typical Meteorological Year 3 (TMY3) weather files [44], and used mid-hour solar positions computed with the Measurement and Information Data Center Solar Position and Intensity (MIDC SOLPOS) Calculator provided by the National Renewable Energy Laboratory [45]. We then calculated in each season (e.g., summer = June/July/August) the variation with solar altitude of the cumulative fraction of wall-incident solar energy in 17 climates across the United States (ESM Figure A-3).

To illustrate, consider summer sunlight in Fresno, CA. About 85%, 37%, 35%, or 1% of the beam radiation incident on a north, east, west, or south wall, respectively, arrives when the solar altitude angle is less than or equal to 30° (Figure 3). Since the incidence angle of beam radiation striking a wall will always equal or exceed the solar altitude angle, less than 37% of the beam radiation striking the east or west wall, and essentially none of that striking the south wall, will do so at an incidence angle less than or equal to 30°. While most beam radiation striking the north wall will do so at solar altitude angles less than or equal to 30°, the north wall receives little beam sunlight.

ESM Table A-1 summarizes by U.S. climate and wall direction the distribution with solar altitude angle of beam sunlight incident in summer.

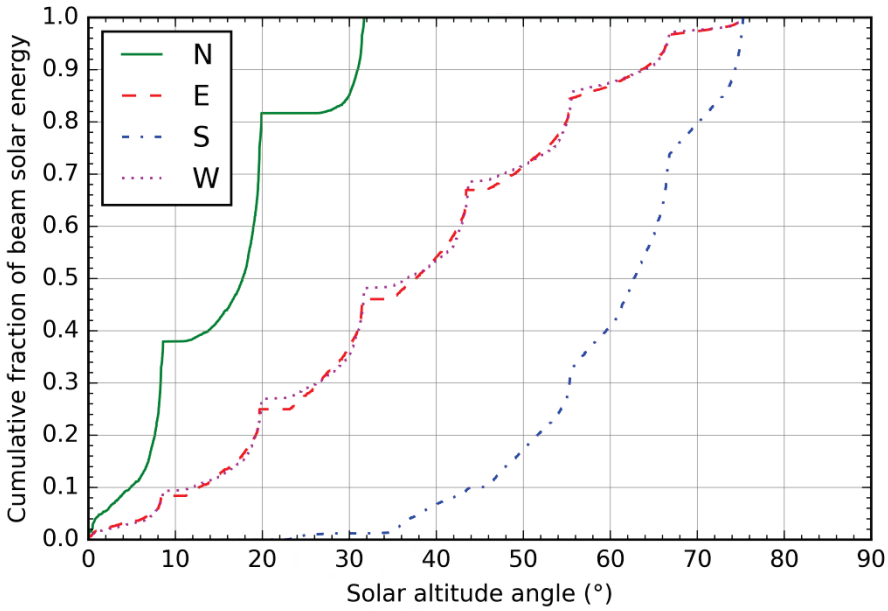

Figure 3. Variation with solar altitude angle of the cumulative fraction of beam solar energy incident on an isolated north (N), east (E), south (S), or west (W) wall in Fresno, CA in summer.

3.3 Vertical surface retroreflection vs. solar altitude angle

The preceding analysis indicates that systems that retroreflect only near-normal light may not work well when applied to south, east, and west walls.

Consider beam sunlight incident on the vertical symmetric two-surface retroreflector shown in Figure 4. A beam of altitude angle $\alpha < 45°$ in the plane of page will strike face 1 at incidence angle $\theta_1 = \alpha + \gamma = \alpha + (90° - \beta) = 45° + \alpha$. The beam reflected from face 1 will strike face 2 at incidence angle $\theta_2 = 180° - 90° - \theta_1 = 45° - \alpha$. The beam reflected from face 2 will be anti-parallel to the original solar beam, completing the retroreflection.

3.3.1 Case 1: Metal mirror faces

If each surface is metal mirror, the system will retroreflect beam sunlight incident on face 1 when $\alpha < 45°$; retroreflect beam sunlight originally incident on face 2 when $\alpha = 45°$; and reflect specularly upward, but not to its origin, beam sunlight originally incident on face 2 when $\alpha \neq 45°$. The latter flux will go directly to the sky when $\alpha < 45°$, or to the sky via face 1 when $\alpha > 45°$.

3.3.2 Case 2: Transparent faces

If each surface is made of the same transparent material with $n \geq 1.5$, face 1 will exhibit TIR for $\alpha < 45°$ because the beam incidence angle $\theta_1 = 45° + \alpha$ will always exceed the material's critical angle in air, θ_c (Figure 5). However, the beam reflected from face 1 will be reflected by face 2 only if $\theta_2 = 45° - \alpha$

exceeds θ_c. The maximum solar altitude α_{max} at which face 2 will total internally reflect the beam from face 1 beam ranges from 3.2° for low-index glass (n=1.5) to 20.4° for diamond (n=2.4) (ESM Table A-2). When $\alpha_{max} < \alpha < 45°$, beam light reflected from face 1 will pass through face 2. Meanwhile, beam sunlight originally incident on face 2 will strike at angle $\theta_2 = 45° - \alpha$. If $\theta_2 < \theta_c$, it will pass through face 2. Otherwise, it will be reflected specularly upward, in some cases striking face 1. Reflected light that strikes face 1 will be reflected to the sky since $\theta_1 = 45° + \alpha > \theta_c$. Thus, beam sunlight incident originally incident on either face 1 or face 2 will pass through face 2 when $\theta_2 = 45° - \alpha \leq \theta_c$, or $\alpha \geq 45° - \theta_c$.

Inspection of the 5° altitude columns in sections b-d of ESM Table A-1 indicates that if made of low-index glass or plastic ($n = 1.5$, $\theta_c = 3.2°$), this system will transmit, rather than retroreflect, nearly all beam sunlight incident on an east, south, or west wall in summer.

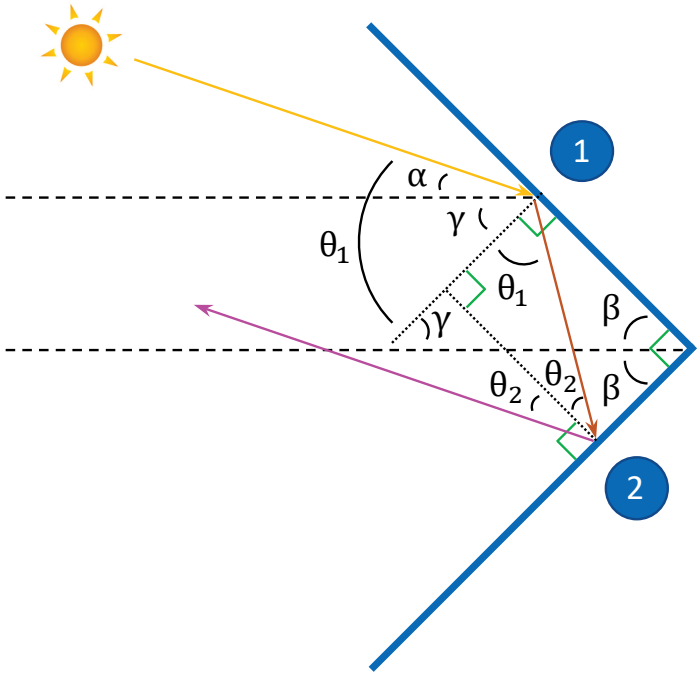

Figure 4. Angles of incidence and reflectance at faces of a vertical symmetric two-surface retroreflector (isosceles right triangle formed by orthogonal faces 1 and 2 and their undrawn vertical hypotenuse; β=45°).

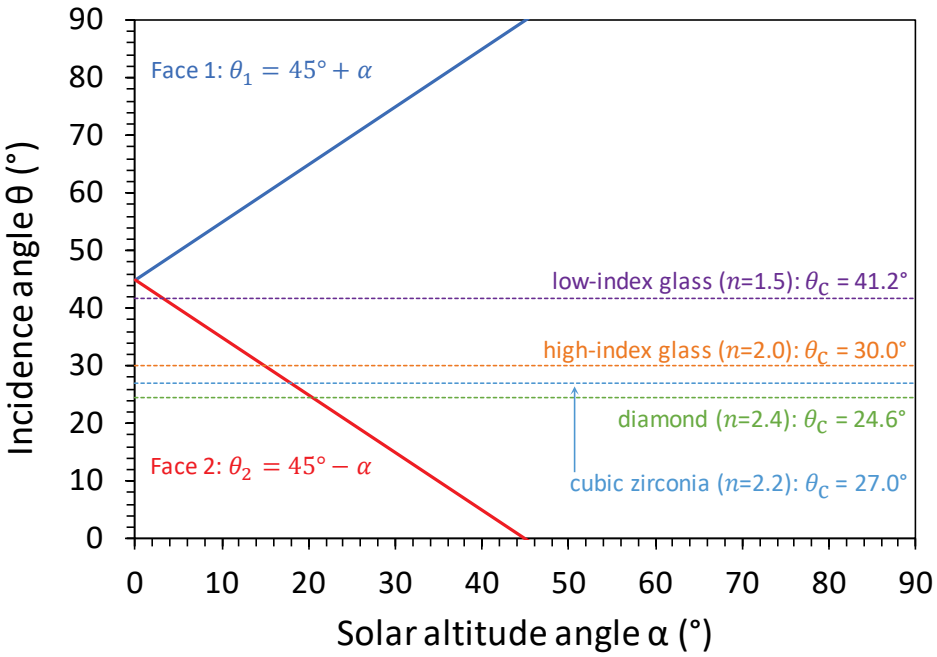

Figure 5. Angles of incidence on faces 1 and 2 in the vertical retroreflector system (Figure 4) when downwelling beam sunlight strikes face 1 and beam light reflected from face 1 strikes face 2. Shown for reference are the critical angles for various clear windows in air; total internal reflection will occur only when incidence angle θ exceeds critical angle θ_c.

3.4 Ray-tracing simulations of 2-D vertical retroreflectors

To screen wall-retroreflector designs, we used the open-source web application Ray Optics Simulation [46] to simulate a variety of 2-D vertical retroreflectors, including four that use open metal mirrors without prisms, four that use prisms without mirror backings, and four that use prisms with metal mirror backings. Glass was modeled as non-absorbing, and mirrors were assumed to reflect all incident light specularly.

3.4.1 Configurations

Each "symmetric" design comprises an array of pairs of equal length faces forming an isosceles right triangle with a vertical hypotenuse and 45° acute angles. Each "asymmetric" design comprises an array of pairs of unequal length faces (upper face length 5, lower face length 3.3, in arbitrary units) forming a right triangle with a vertical hypotenuse and acute angles of 33.5° (top) and 56.5° (bottom). Low and high-index glasses follow the specifications of ESM Table A-2.

We simulated the following 12 configurations:

a) Symmetric open mirrors, where light passes from air to ideal metal mirrors.

b) Symmetric open mirrors behind a low-index glass vertical window, to keep the mirrors clean.

c) Asymmetric open mirrors.

d) Asymmetric open mirrors behind a low-index glass vertical window.

e) Symmetric low-index glass right triangular prisms.

f) Symmetric low-index glass right triangular prisms with ideal metal mirror backing replacing the glass-air interface.

g) Asymmetric low-index glass right triangular prisms.

h) Asymmetric low-index glass right triangular prisms with ideal metal mirror backing.

i) Symmetric high-index glass right triangular prisms.

j) Symmetric high-index glass right triangular prisms with ideal metal mirror backing.

k) Asymmetric high-index glass right triangular prisms.

l) Asymmetric high-index glass right triangular prisms with ideal metal mirror backing.

3.4.2 Results

Figure 6 shows the paths of beams incident from solar altitude angles of α = 0, 15, 30, 45, 60, and 75°. The following observations are limited to these six altitudes angles.

Prisms:

- As predicted in Section 3.3.2, design *e* retroreflects only at α = 0° and design *i* retroreflects only at α = 0, 15, and 30°. The retroreflection at α = 30° by design *i* is simply specular reflection.
- Design *g* does not work.
- Design *k* fares poorly at α = 0°, provides mixed results at α = 30°, and works well at α > 30°.
- Mirror backings (designs *f*, *h*, *j*, and *l*) help a bit, but reflect some light downward.

Open mirrors:

- Design *a* provides a combination of retroreflection and not-to-origin upward reflection.
- Design *c* fares poorly at α = 0°, provides mixed results at α = 30°, and works well at α > 30°.
- Placing the mirrors behind a vertical window (designs *b* and *d*) has little effect.

From these analyses we conclude that design *a* (symmetric open mirrors) is the logical starting point for prototype fabrication, and that it can kept clean behind a low-index window (design *b*) without performance penalty.

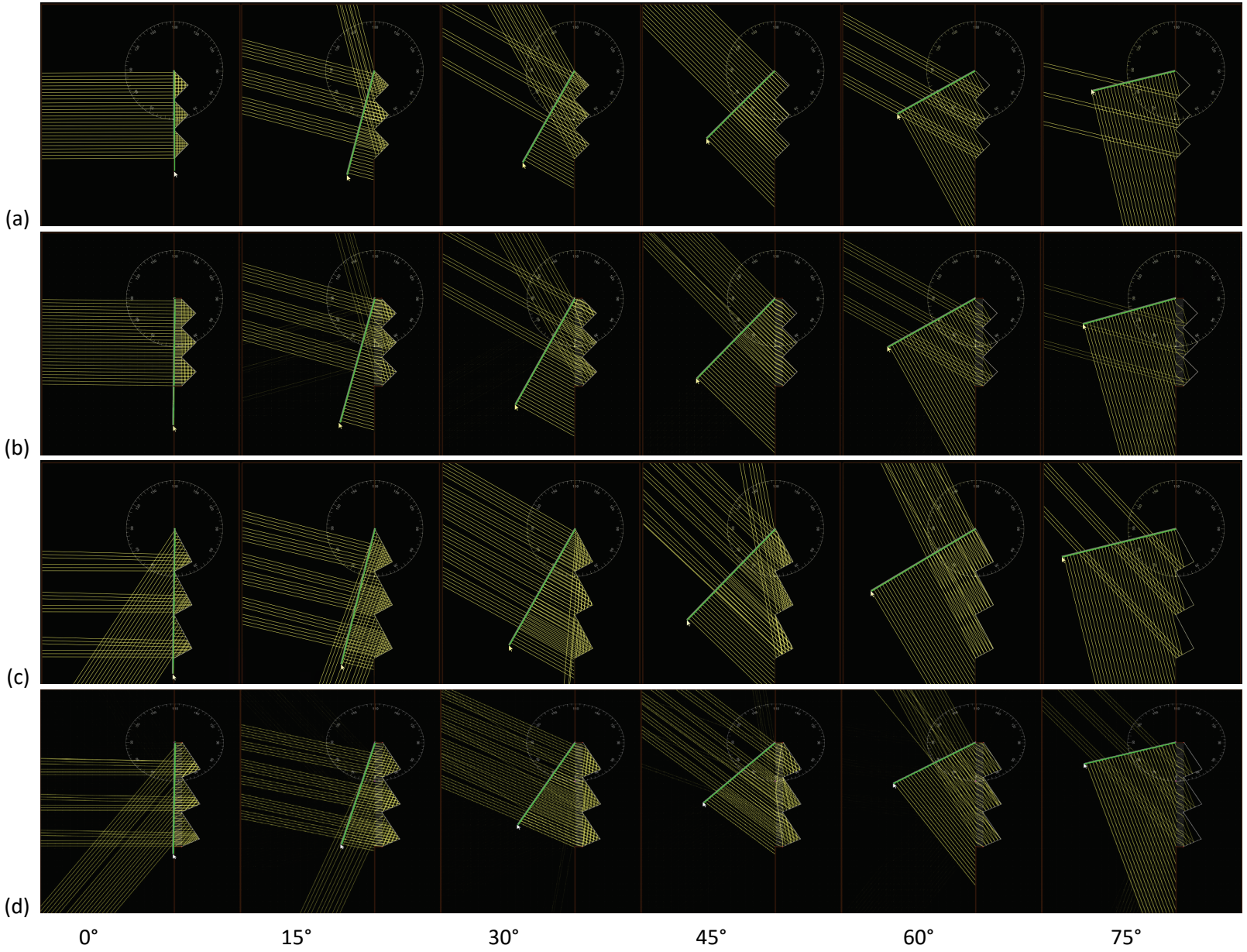

Figure 6. Reflection of beam light as a function of beam altitude angle, shown for a variety of two-surface retroreflectors. Shown here: (a) symmetric open mirrors; (b) symmetric open mirrors behind a low-index glass window (n=1.5); (c) asymmetric open mirrors; (d) asymmetric open mirrors behind a low-index glass window (n=1.5).

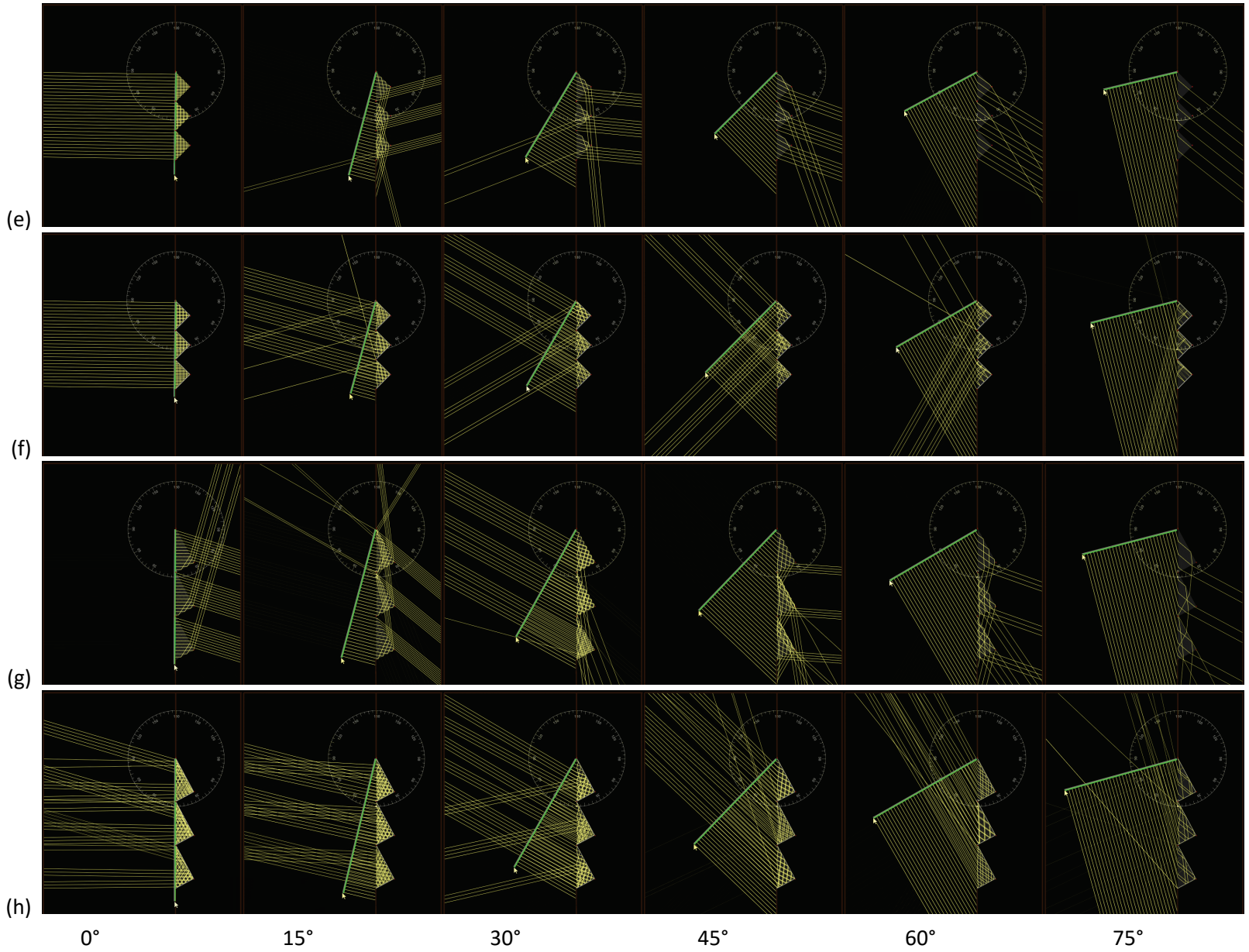

Figure 6 (continued). Shown here: (e) symmetric low-index glass (n=1.5) right triangular prisms; (f) system *e* plus mirror backing; (g) asymmetric low-index glass (n=1.5) right triangular prisms; (h) system *g* plus mirror backing.

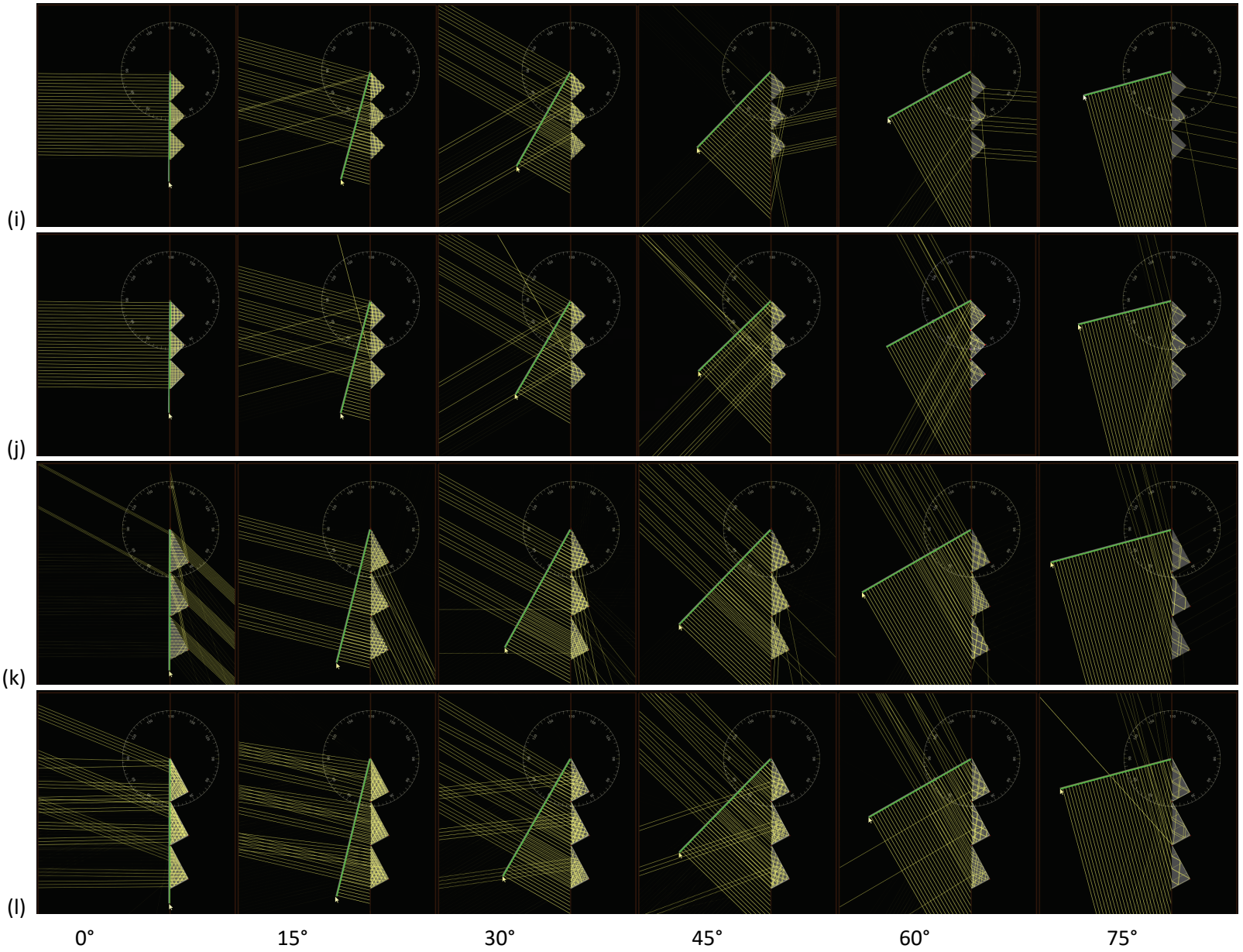

Figure 6 (continued). Shown here: (i) symmetric high-index glass (n=2.0) right triangular prisms; (j) system *i* plus mirror backing; (k) asymmetric high-index glass (n=2.0) right triangular prisms; and (l) system *k* plus mirror backing.

4 Instrumentation

We assessed near normal-hemispherical and near normal-specular reflectances with a commercial UV-vis-NIR spectrophotometer, and retroreflection with two instruments: a simple, monochromatic goniometer built by Lawrence Berkeley National Laboratory (LBNL), and an advanced solar spectral goniometer designed and operated by Dexerials.

4.1 Spectrophotometer

A Perkin-Elmer Lambda 900 UV-vis-NIR spectrometer equipped with a 150 mm Labsphere integrating sphere was used to measure near normal-hemispherical spectral reflectance (250 – 2,500 nm at interval 5 nm) following ASTM E903-12: Standard Test Method for Solar Absorptance, Reflectance, and Transmittance of Materials Using Integrating Spheres [47]. Specular reflectance was obtained by subtracting reflectance measured with the sphere's specular reflectance port open from that measured with it closed. Combining a 0.5% fractional uncertainty in the reflectance of the Labsphere Spectralon SRS-99 reflectance standard (nominal absolute spectral reflectance near 0.99) with a 0.01 absolute uncertainty induced by the use of this diffusely reflecting standard to characterize specular reflectance [47] yields an absolute uncertainty of about 0.011 in measurement of solar spectral reflectance.

Solar reflectance R_{sol} (300 – 2,500 nm), ultraviolet reflectance R_{uv} (300 – 400 nm), visible reflectance R_{vis} (400 – 700 nm), and near-infrared reflectance R_{nir} (700 – 2,500 nm) were calculated by weighting spectral reflectance with an air mass 1 global horizontal (AM1GH) solar spectral irradiance [42,48].

4.2 Simple laser-and-paper goniometer

The simple goniometer comprises a laser pointer shining vertically upward through a small (about 2 mm) central hole in the bottom of an opaque tray (Figure 7), illuminating an approximately 2 mm measurement spot on a downward-facing test surface mounted on a rotatable rod 20 mm above the light source. As both the tray and laser pointer are fixed in place, the test specimen can be rotated to vary the angle of incident laser light (Figure 8). Light reflecting off the test surface forms a pattern on the surface of the tray bottom, which bears a grid of concentric circles centered on the light source. A camera angled downwards on the tray captures an unobstructed image of the reflection pattern within these grid rings. This pattern represents the combination of specular, diffuse, and retroreflection for a given pairing of illumination incidence angle and test specimen orientation.

In the absence of a mechanism for measuring or controlling rotation of the rod, the circular grid provides a quick method of identifying the illumination incidence angle corresponding to a rotated test specimen. Given that angle of incidence equals angle of specular (Fresnel) reflection, the grid rings use the location of specularly reflected laser light as a marker for incidence angle. Fifteen grid rings are drawn at specular reflection locations corresponding to a set of fifteen incidence angles (5° to 75° in 5° increments). This circular grid graphic is shown in ESM Figure A-4.

Analysis of the reflection patterns produced by the simple goniometer requires differentiating between specular reflection and retroreflection. A light spot corresponding to specularly reflected laser light is similar in size to the incident beam and moves as the test surface rotates. Retroreflected light remains near the light source hole regardless of specimen rotation. At large incidence angles the retroreflected and specularly reflected light are well separated.

The angle of Fresnel (first-surface) reflection equals the angle of incidence on the specimen. The intensity of the retroreflection (if any) can be compared to that of the Fresnel reflection computed from Fresnel's equations [49] (ESM Table A-3).

The angular distribution of reflected light within the rings gauges the potential for the test specimen to retroreflect or specularly reflect light. Retroreflected light that is distributed over a smaller or larger area of the circular grid indicates a narrower or wider cone of retroflection. Retroreflective materials ideal for our application will exhibit bright retroreflection (relative to specular reflection) distributed over a narrow cone.

This version of the simple goniometer was assembled at no cost with existing consumer-grade materials, and consequently has several limitations. The output of the battery-powered laser pointer was not controlled, so no conclusions can be drawn about brightness differences observed in different photographs. In cases where the dynamic range of the reflection pattern exceeded that of the camera, overexposure and detail loss prevented quantitative brightness comparisons even within the same photograph. Angling the camera to avoid obstruction of the full reflection pattern instead introduced geometric distortion, which stymied attempts at straightforward digital image analysis. In this paper, our interpretation of simple goniometer images will rely primarily on visual assessments of brightness differences. All these limitations, however, can likely be mitigated through adjustments to design or materials.

Various non-retroreflective specimens (ESM Figure A-5) and retroreflective specimens (Table 1; Figure 9) were tested using the simple goniometer. The three non-retroreflective specimens are either mirrors or mirror-like surfaces exhibiting varying degrees of specular and diffuse reflection. The polished aluminum panel has some degree of small-scale surface roughness—as is evident from faintly visible parallel marks—and exhibits the least amount of specular reflection. The metallized Mylar film exhibits the highest degree of specular reflection.

Patterns of light reflection from three of the specimens—a mirror calibration standard, a polished aluminum panel with brush marks, and a Type I white retroreflective safety film—can be seen in Figure 10. All specimens were tilted to obtain an the illumination incidence angle of 70°. Specularly reflected light can be observed as the bright spot at the 70° circular grid ring, while retroreflection can be observed as a relatively wide cone of brightness centered near the laser beam source.

As expected, each specimen yields a specular (Fresnel) reflection, but only the safety film exhibits retroreflection. The intensity of this retroreflection can be compared to that of the Fresnel reflection at

70°, which ranges from 0.04 to 0.30 if the laser beam is polarized, or is 0.17 if the laser beam is unpolarized (ESM Table A-3).

We recommend rotating a linearly polarized laser beam about its axis to orient its electric field perpendicular to the plane of incidence (that containing the surface normal and incident ray). This will raise its Fresnel reflectance to its maximum (s-polarized) value R_S, making it easier to compare retroreflection to Fresnel reflection. The upper and lower images in Figure 10c show maximum and minimum specular reflectances observed when rotating the incident laser beam. The rotations corresponding to these two images were approximately 90° apart.

4.3 Gonio-spectrophotometer

Dexerials' gonio-spectrophotometer (ESM Figure A-6) measures solar spectral bi-directional reflectivity from 350 to 2,350 nm with a fractional uncertainty of about 3%. Its design and operation are detailed by Harima & Nagahama [26,27].

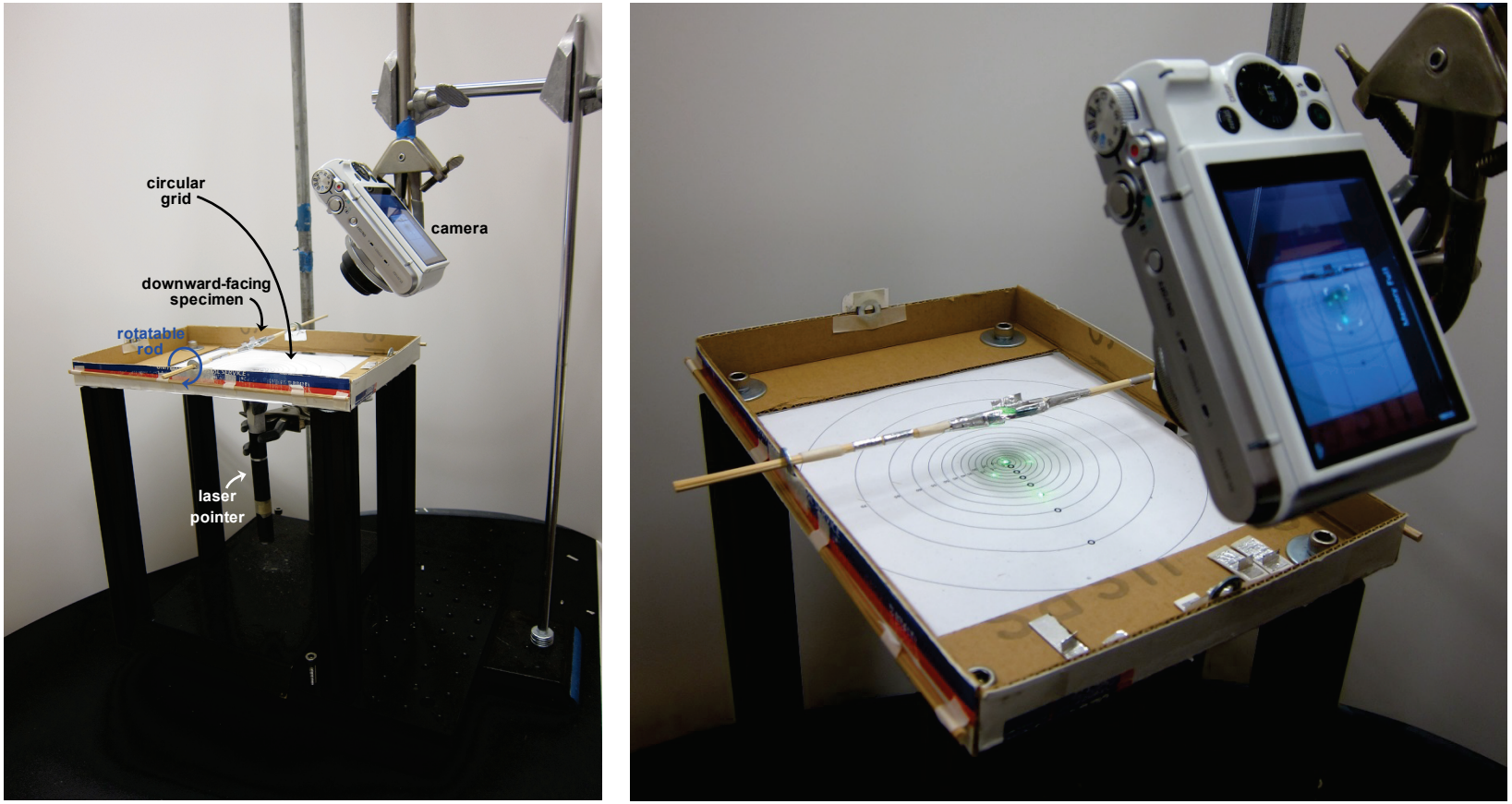

(a) (b)

Figure 7. LBNL built a simple goniometer to compare retroreflection to specular reflection. Shown above: (a) side view of goniometer with laser pointer shining up and camera looking down; (b) top view of goniometer, showing a retroreflective specimen mounted on the turnable rod, central hole admitting laser beam, and concentric rings (5° to 75° in 5° increments) marking angle of reflection.

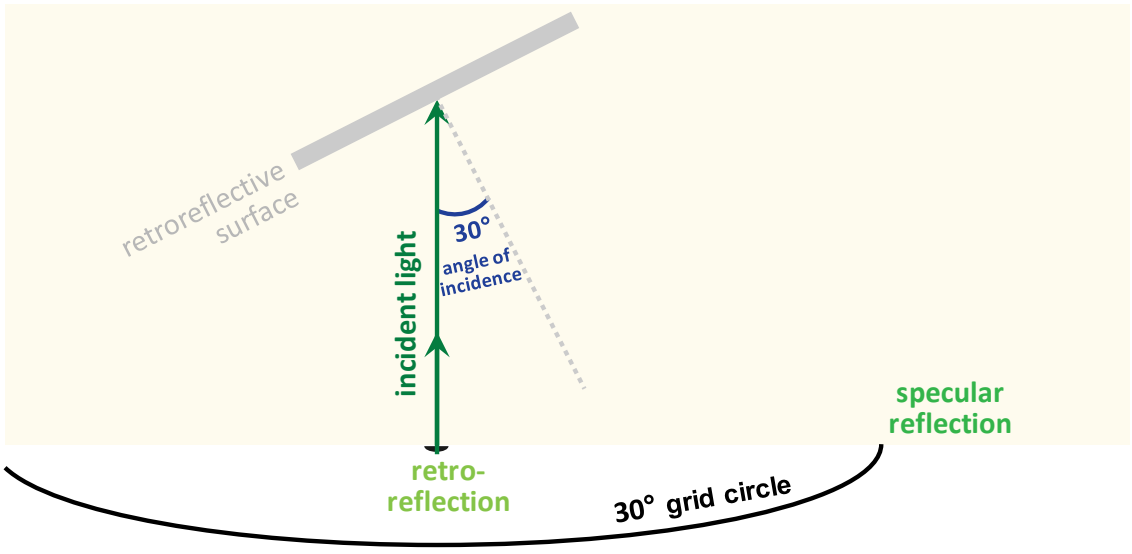

(a)

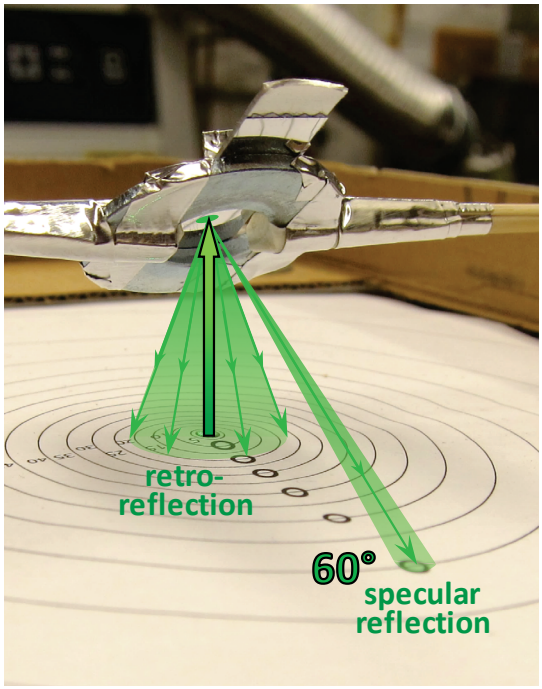

(b)

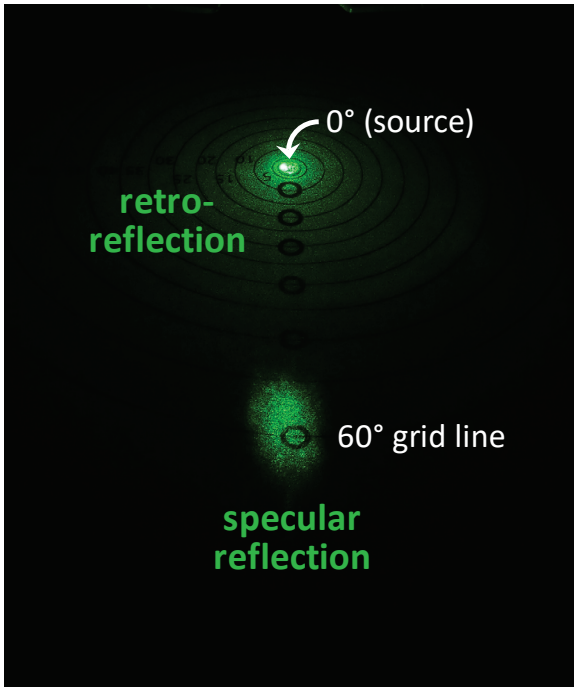

(c)

Figure 8. Schematics showing how retroreflection and specular reflection manifest during usage of the simple goniometer (a, b), and example of a light pattern produced by a retroreflective surface (c). The circular grid rings mark angles of specular reflection (which are equal to the angles of incidence) at intervals of 5 degrees. Panel *c* shows a simple goniometer image of an ASTM D4956 Type I retroreflective safety film tilted to obtain an incidence angle of 60°.

Table 1. Properties of four retroreflective films tested in the simple goniometer. The specimens include three traffic safety films (labeled as Sheetings A, B, and C) and one raised pavement marker.

Product	Specification	Description	Technology	Color
Sheeting A	ASTM D4956 Type I	Engineering-grade flexible sheeting	Enclosed lens glass bead	White
Sheeting B	ASTM D4956 Type III / Type IV	High-intensity prismatic rigid sheeting	Unmetallized microprism	White
Sheeting C	ASTM D4956 Type XI	Super-high efficiency rigid sheeting	Unmetallized cube corner microprism	White
Pavement marker	ASTM D4280 Type B *	Flat retroreflective element embedded in rigid thermoplastic	Microprism	White

* See ASTM International [50].

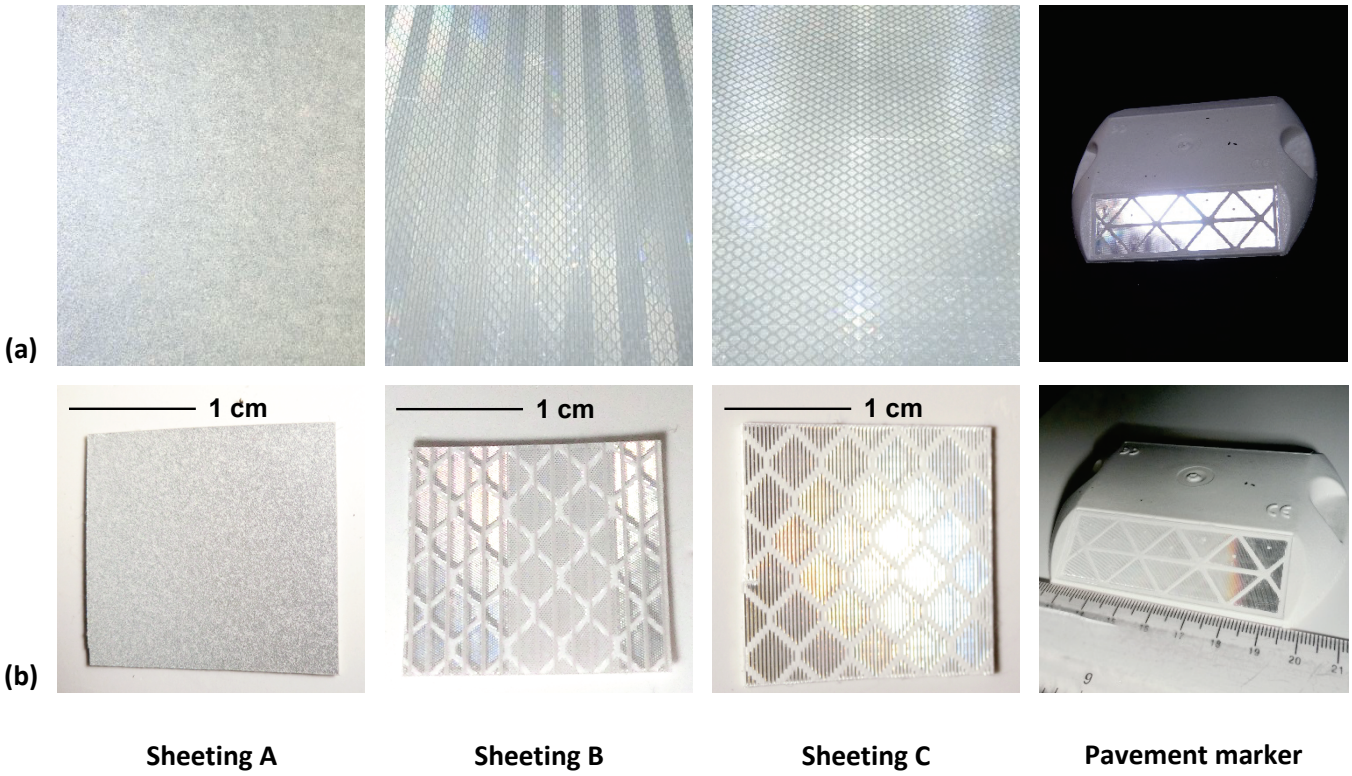

Figure 9. Photos of four retroreflective specimens that were tested in the simple goniometer. The products are displayed in row a, with accompanying close-up views in row *b*. The close-up of the pavement marker includes a centimeter ruler.

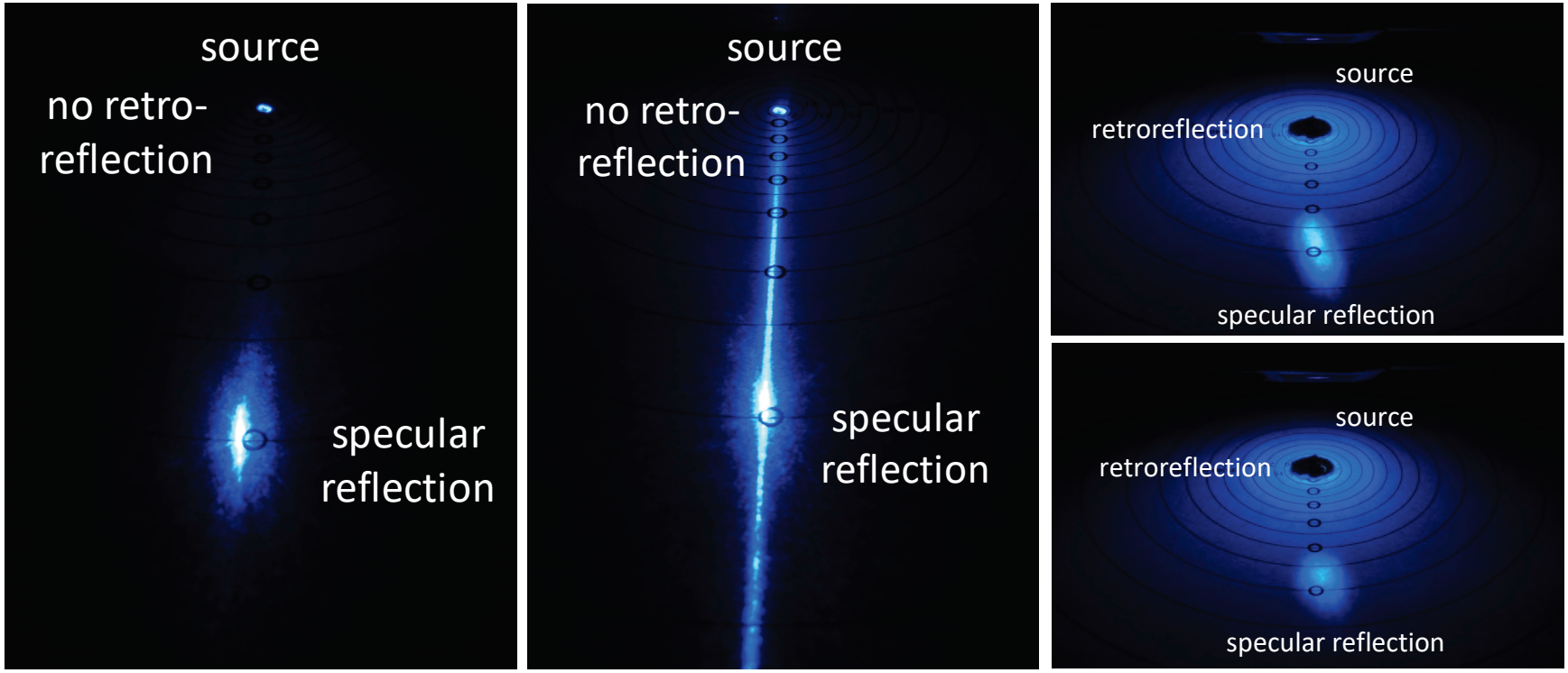

(a) (b) (c)

Figure 10. Simple goniometer images of violet (405 nm) laser light at 70° incidence reflected from two non-retroreflective surfaces (a, b) and one retroreflective surface (c). Panel *a* shows a mirror calibration standard exhibiting purely specular reflection; panel *b* shows a polished aluminum panel exhibiting specular reflection; and panel *c* shows a Type I white retroreflective safety film, exhibiting both specular reflection and retroreflection. Upper and lower images in panel *c* show the maximum and minimum specular reflectances observed when the rotating incident laser beam about its axis.

5 Evaluation of some commercially available retroreflectors

We began by exploring prototypes based on some commercially available retroreflectors, including traffic safety films and bicycle reflectors.

5.1 Solar spectral specular reflectance of mirrorlike surfaces

In principle, a transparent surface exhibiting total internal reflection (TIR) or a metal mirror can provide strong specular reflection over most or all of the solar spectrum (300 – 2,500 nm). Examples:

- Crown glass (e.g., Schott N-BK7) has a narrow range of real refractive index (n=1.48 – 1.56) over the entire solar spectrum. Its internal transmittance is greater than 0.99 from 400 to 1,500 nm, greater than 0.93 from 1,500 to 2,000 nm, and 0.66 to 0.93 at wavelengths longer than 2,000 nm [51], minimizing solar absorption within a glass prism shaped to provide TIR.

- An optical-grade mirror calibration standard can specularly reflect nearly 90% of incident sunlight (curve B in Figure 11).

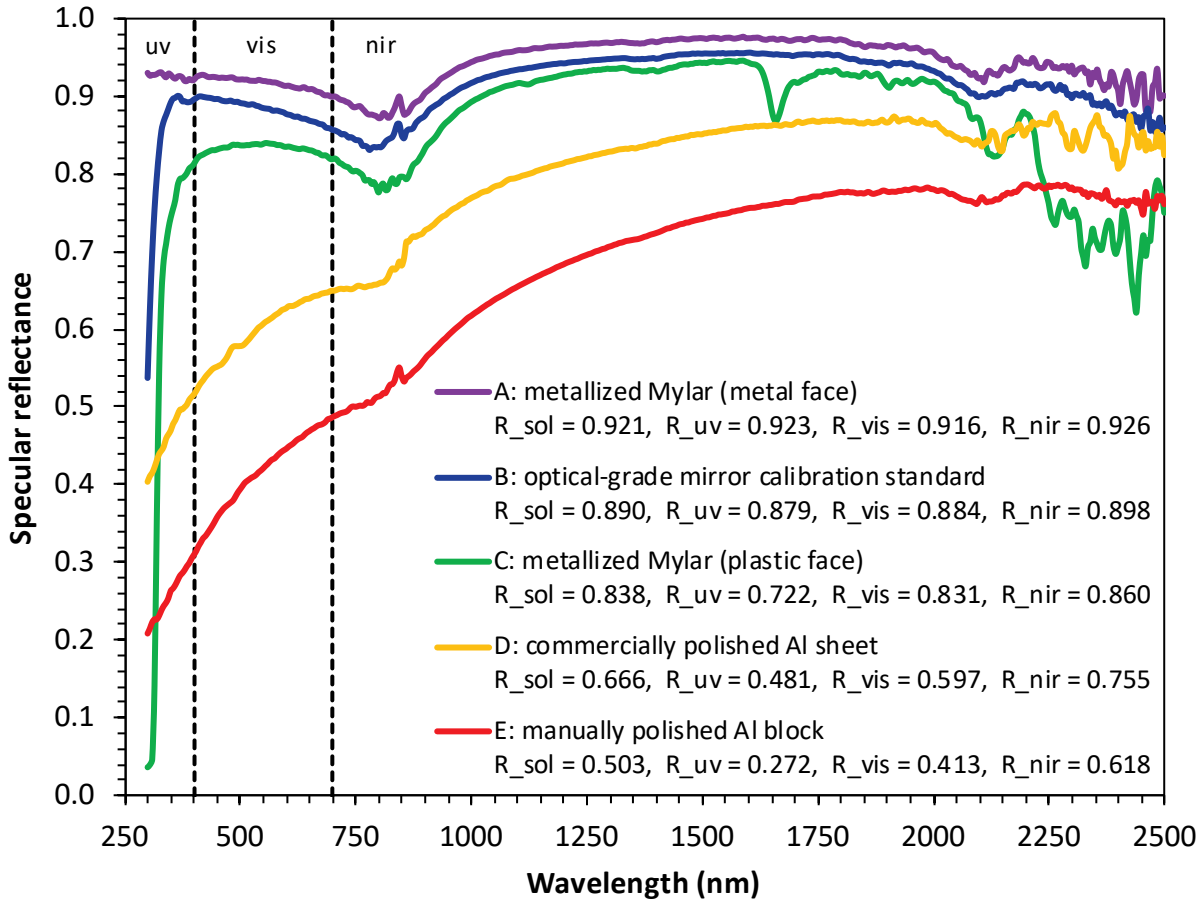

Figure 11. Near normal-specular solar spectral reflectances of five mirrorlike systems, including (a) the metal face of aluminized Mylar, (b) an optical-grade mirror calibration standard, (c) the plastic face of aluminized Mylar; (d) a commercially polished aluminum sheet, and (e) a manually polished block of aluminum.

5.2 Safety films

We tested four retroreflective specimens using the simple goniometer. Three specimens (identified as Sheetings A, B, and C) are adhesive-backed traffic safety films, and one specimen is the retroreflective element of a raised pavement marker. These specimens are described in Table 1 and photographed in Figure 9.

Retroreflection by Type I glass bead materials—such as Sheeting A—is insensitive to orientation. This is not the case for prismatic-type retroreflective materials. For these "azimuthally sensitive" specimens, we performed tests in two perpendicular orientations, arbitrarily assigned with reference to primary pattern lines on the specimen surface. In what is labeled "orientation 1", the specimen is positioned such that its primary pattern lines run perpendicular to the plane of incident laser light. In "orientation 2", the

specimen is rotated 90° such that its pattern lines instead run parallel to the plane of incidence (ESM Figure A-7).

Specimens were prepared for measurement by applying multiple layers of white tape to the back side to ensure opacity. Additionally, specimens were positioned such that the incident laser beam avoided, as much as was possible, major nonlinear surface pattern lines. The retroreflective element on the pavement marker was detached from the marker's plastic body for testing.

Examination in the simple goniometer of retroreflections and Fresnel reflections (Figure 12) from several retroreflective sheets (Table 1) shows that across the board, retroreflection looks dimmer than Fresnel reflection. This could indicatae that in all tested specimens, retroreflection is weaker than Fresnel reflectance—that is, less than 0.09 at incidence angles up to 45°, and less than 0.30 at incidence angles of up to 70° (ESM Table A-3)—but this interpretation will ultimately require quantitative corroboration because that retroreflection is spread over a larger area. The modest retroreflection observed at large incidence angles (50–70°) suggests that safety films may not be ideal materials for retroreflective cool walls, but quantitative tests—e.g., measurement of bi-directional solar reflectivities—may be warranted.

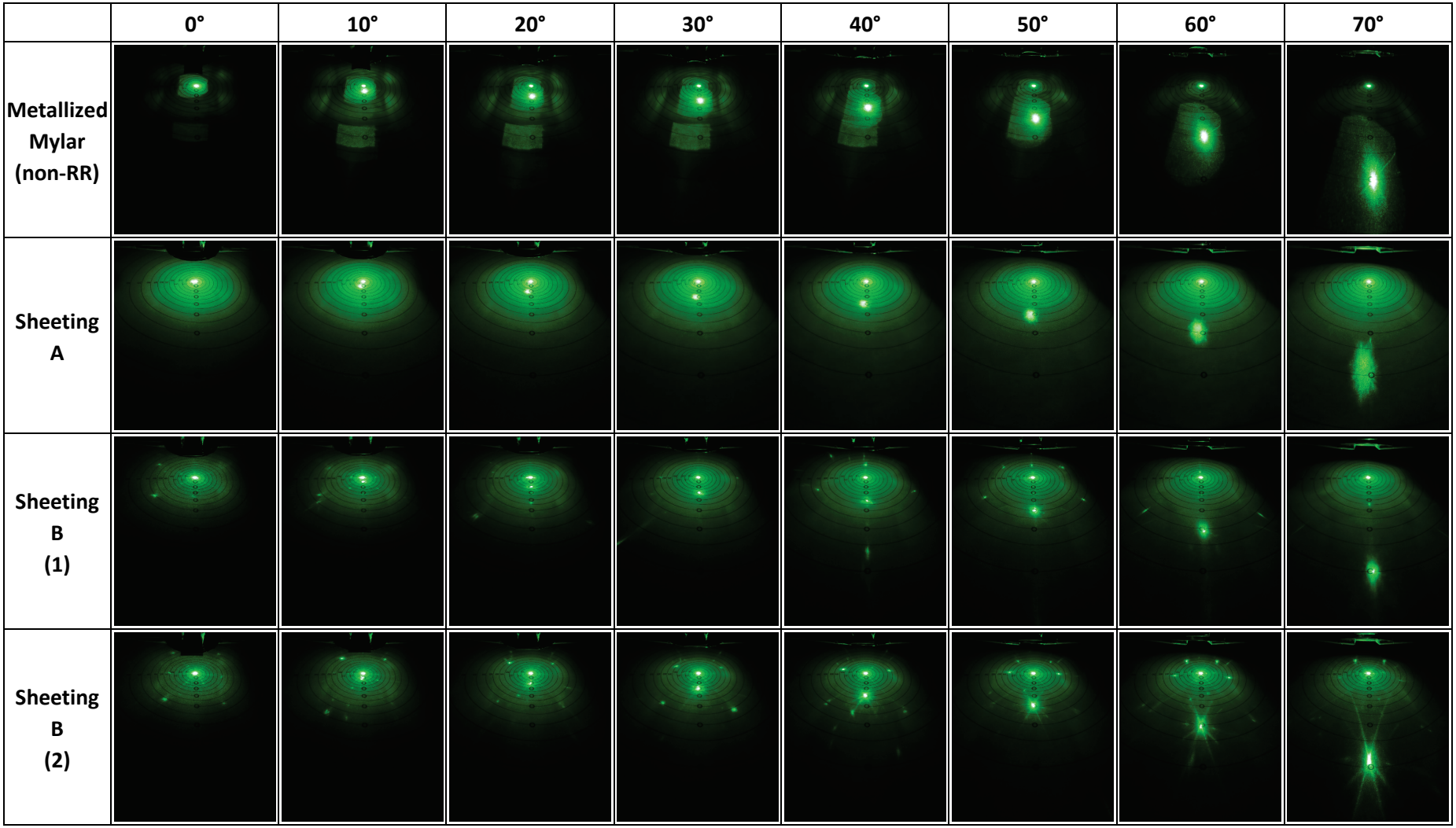

Figure 12. Simple goniometer images of 0°, 10°, 20°, 30°, 40°, 50°, 60°, and 70° incident green (532 nm) laser light reflected from a non-retroreflective reference surface, 3 retroreflective safety films, and a retroreflective element detached from a road pavement marker. Sheetings B and C, which are azimuthally sensitive, were tested in two perpendicular orientations. In all tests, the laser beam was rotated about its axis to maximize specular reflection at 15° incidence. One spot measurement was imaged per combination of specimen, incidence, and orientation.

	0°	10°	20°	30°	40°	50°	60°	70°
Sheeting C (1)	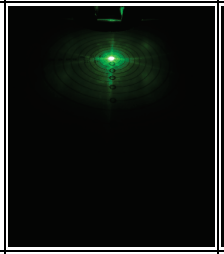	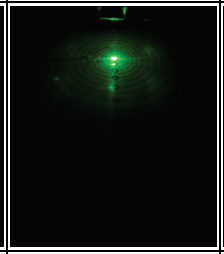	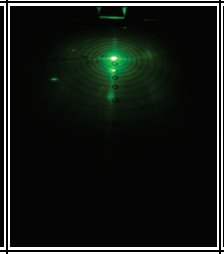	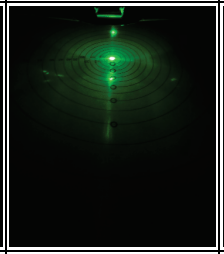	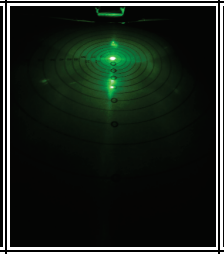	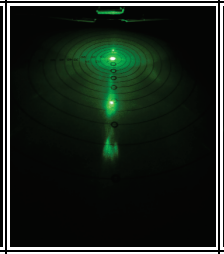	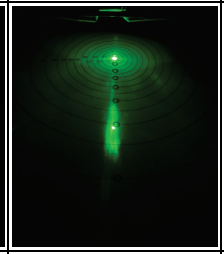	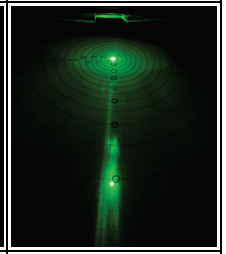
Sheeting C (2)	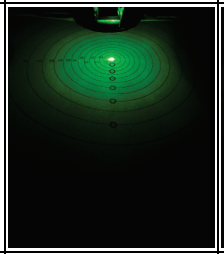	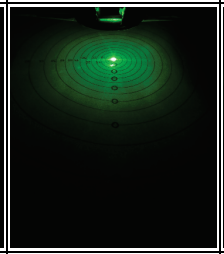	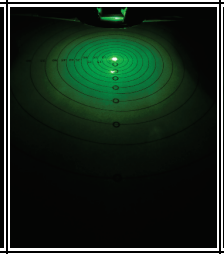	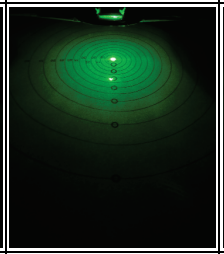	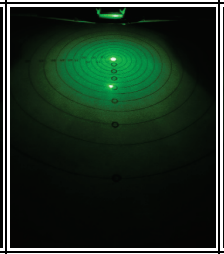	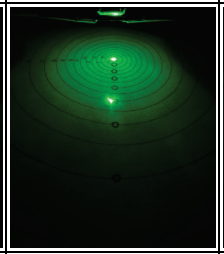	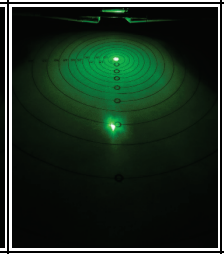	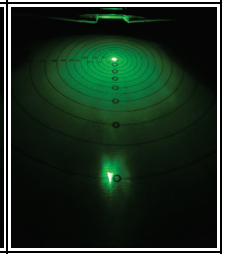
Pavement marker	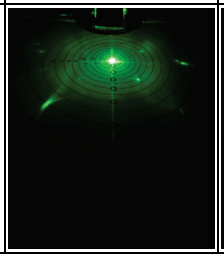	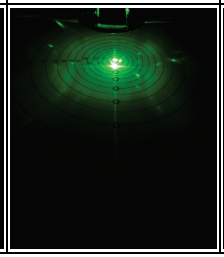	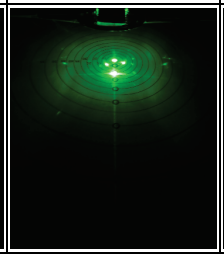	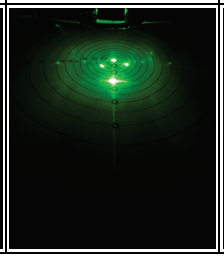	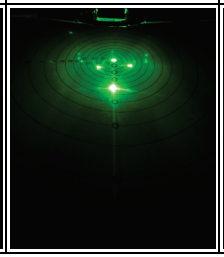	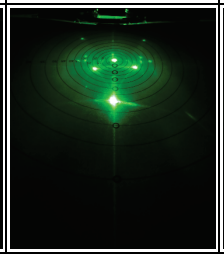	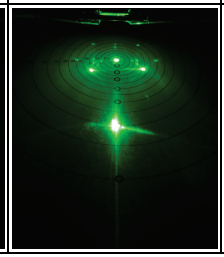	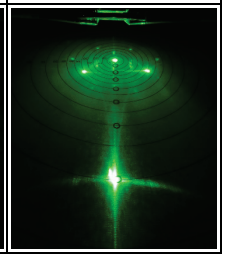

Figure 12 (continued).

5.3 Bicycle retroreflector

We measured the retroreflectance of several specimens of a clear prismatic bicycle reflector in three conditions:

a) bare (Figure 13, left and middle segments in each photo);

b) with a third of the rear coated with LO/MIT low-emittance radiant-barrier paint (Figure 13, right segment in each photo); and

c) with about 0.4 μm of aluminum sputtered on the rear (Figure 14).

Specimen *b* was abandoned after inspection with the simple goniometer indicated that the LO/MIT coating did not enhance retroreflection.

LBNL measured the near normal-hemispherical solar spectral reflectances of the two remaining two specimens, *a* and *c* (Figure 15). Dexerials then measured their bi-directional solar spectral reflectivities in its advanced goniometer, and computed visible (400 – 700 nm) and near-infrared (700 – 2,350 nm) broadband reflectances from the air mass 1.5 normalized spectral distribution of global solar radiation tabulated in ISO Standard 9050:2003: Glass in Building—Determination of Light Transmittance, Solar Direct Transmittance, Total Solar Energy Transmittance, Ultraviolet Transmittance and Related Glazing Factors [52].

Figure 16 shows the visible and near-infrared (NIR) bi-directional reflectivities of the bare reflector (panel a) and the aluminum coated reflector (panel b). Retroreflection from each specimen is evident at incidence angles of 15 and 30°, with a small hint of retroreflection at 45° from the coated specimen. In each case the magnitudes of the visible and NIR retroreflectors are similar, and diminish as incidence angle increases. The aluminum coating increased Fresnel reflection and reduced retroreflection. Since retroreflection essentially vanishes at incidence angles exceeding 30°, these specimens do not seem promising for application to walls.

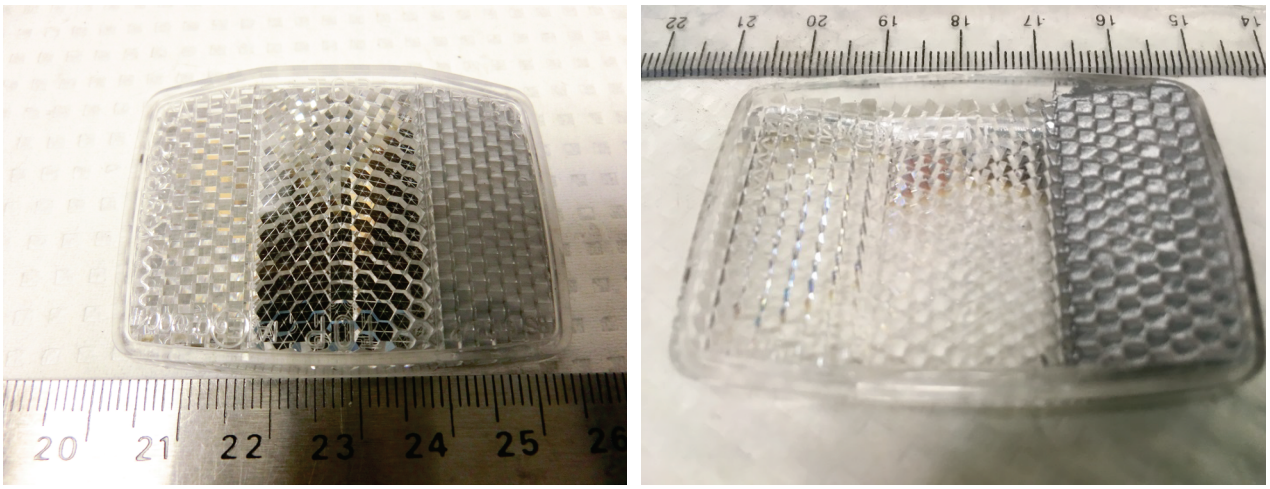

(a) front (b) back

Figure 13. Front and back faces of a clear plastic bicycle retroreflector showing right third of back surface coated with LO/MIT low-emittance radiant barrier paint. Rulers are marked in centimeters.

(a) front (b) back

Figure 14. Front and back faces of another clear plastic bicycle reflector with about 0.4 μm of aluminum sputtered on its back.

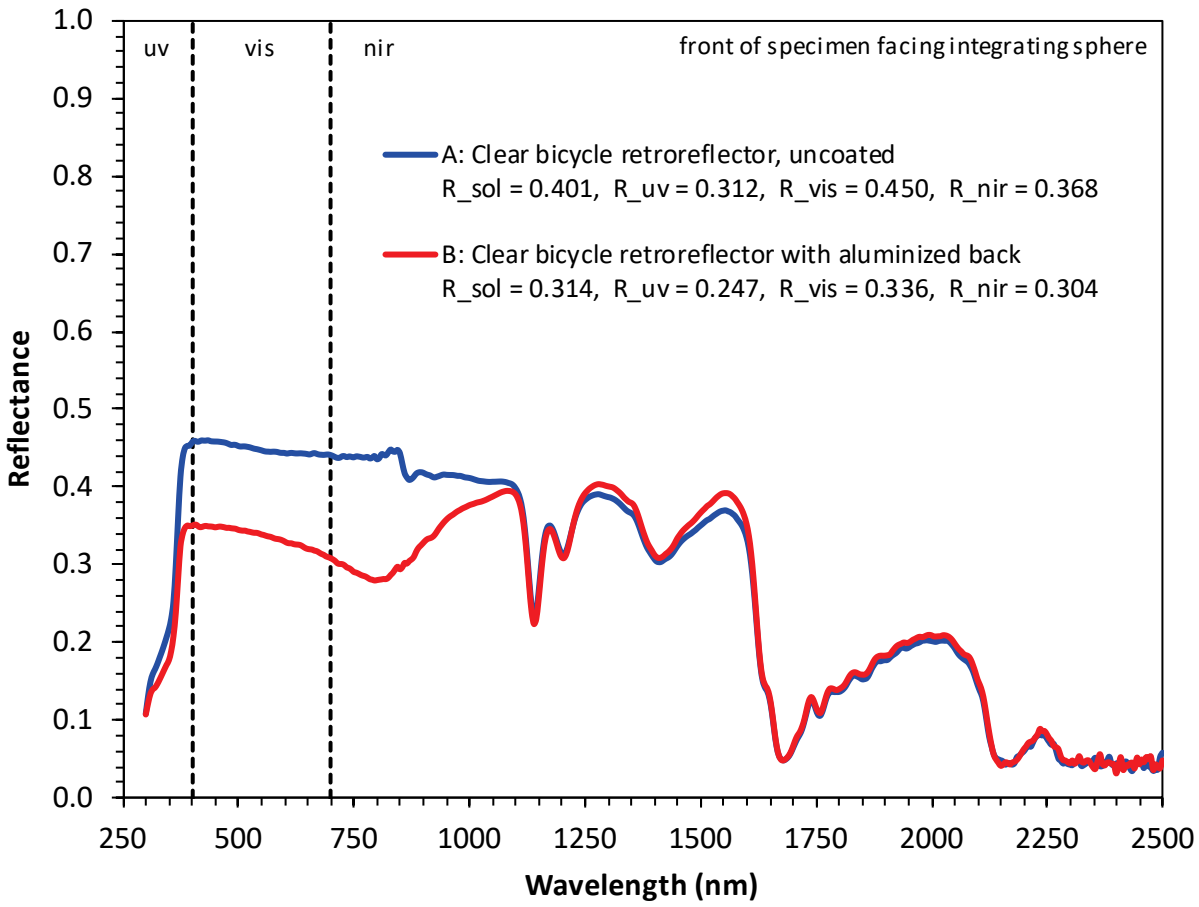

Figure 15. Near normal-hemispherical solar spectral reflectance of front of bicycle retroreflector (A) before and (B) after sputtering aluminum on its back surface.

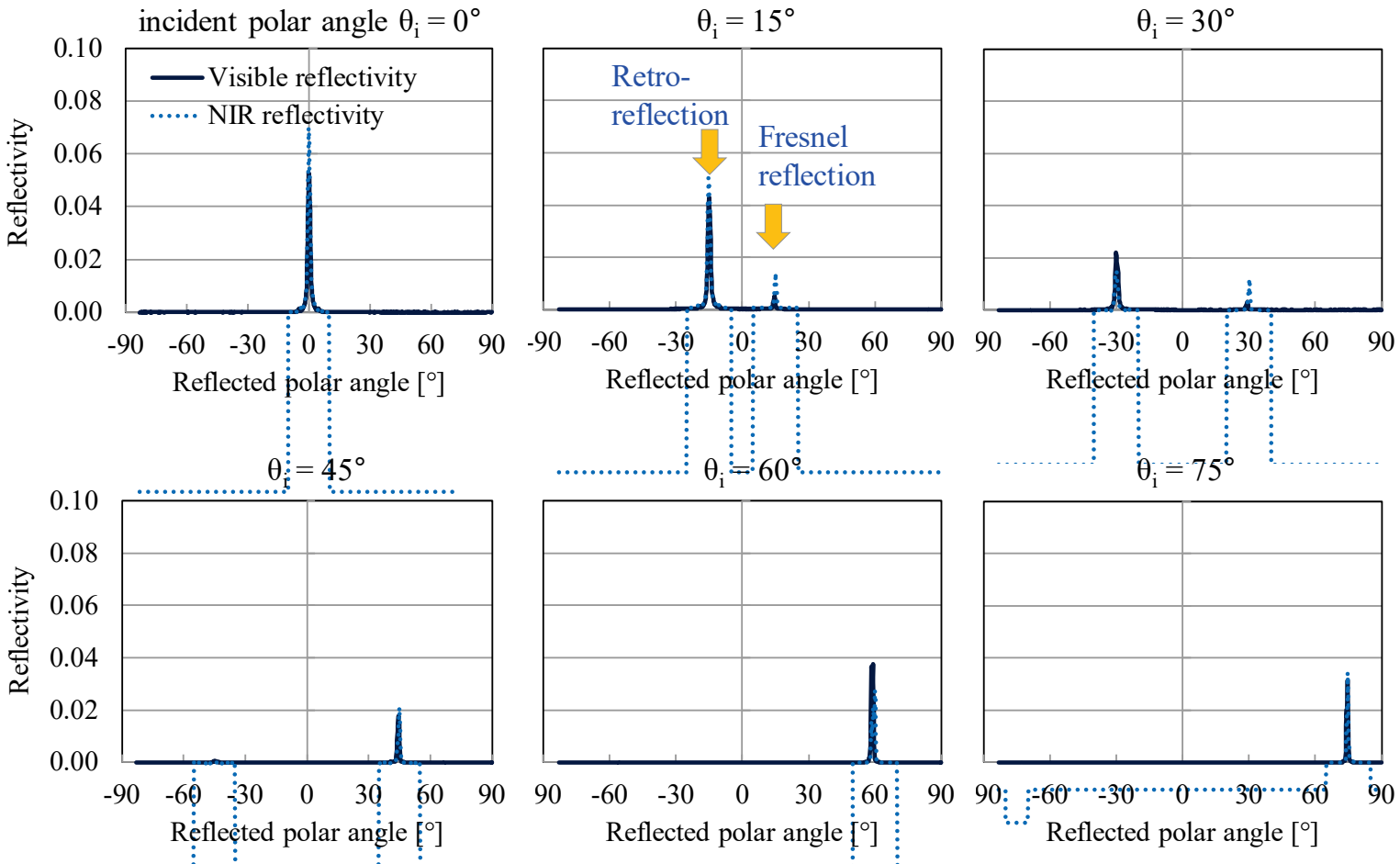

(a)

Figure 16. Broadband visible and near-infrared bi-directional reflectivities of (a) bare bicycle retroreflector and (b) aluminum-coated bicycle retroreflector.

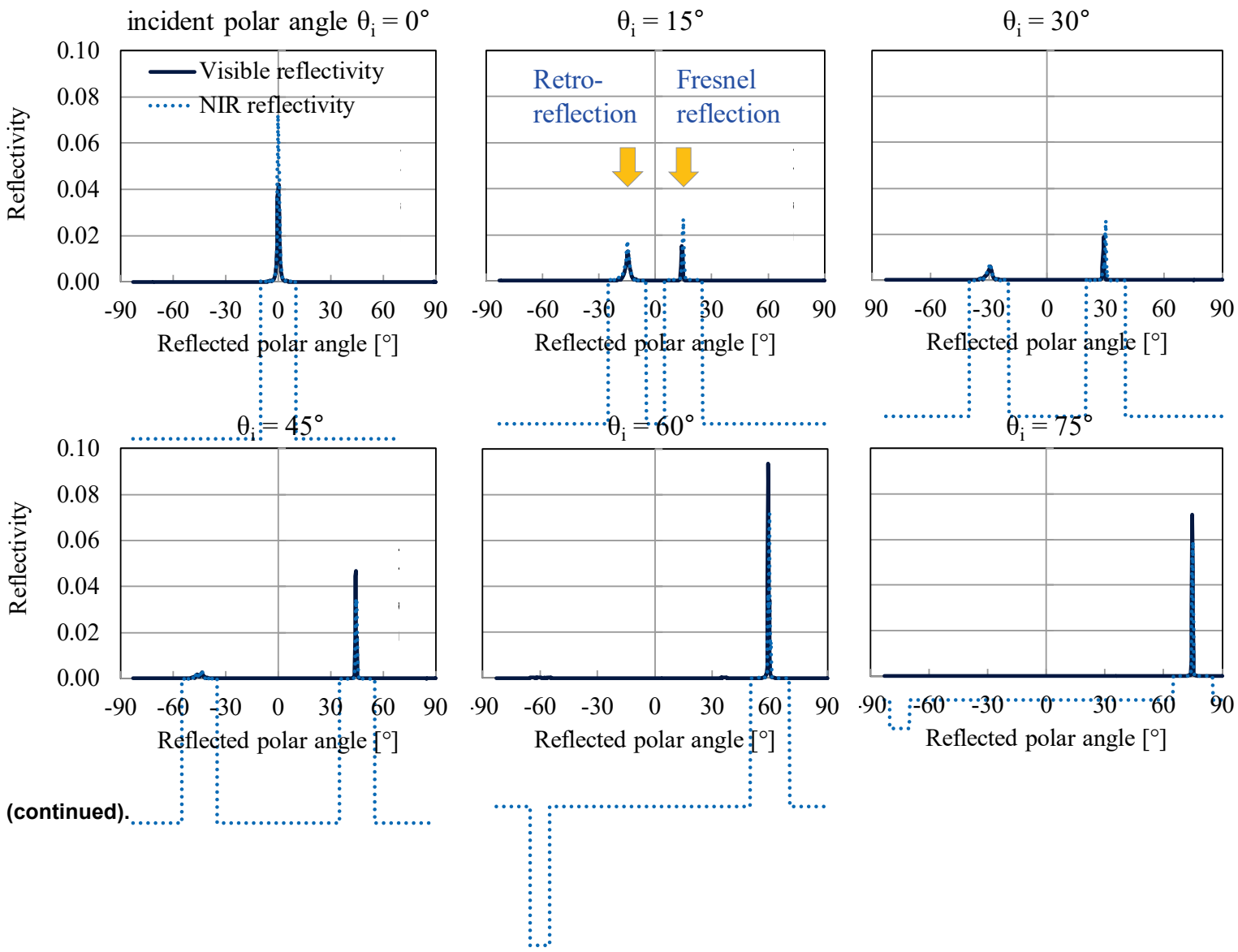

(b)

Figure 16 (continued).

6 Fabrication and evaluation of 2-D mirror retroreflectors

We prepared and characterized several prototype 2-D retroreflectors based on design *a* (symmetric open mirrors) simulated in Section 3.4.

6.1 ABS plastic groove retroflector

We hired a 3-D printing service to fabricate ABS plastic pieces with orthogonal grooves, onto which we planned to sputter a thin coating of aluminum following the same process used to coat the bicycle reflector. However, stairsteps found in the groove faces—an issue that we tried, but failed, to avoid by printing the pieces standing tall—suggested that a thin aluminum coating would also be jagged, and unlikely to provide the specular reflections needed for retroreflection.

6.2 Grooved aluminum block

We used a computer numeric control (CNC) milling machine to cut 2-mm pitch orthogonal grooves in an aluminum block (ESM Figure A-8). The grooves exhibited no retroreflection, so we manually polished them with a buffing wheel and paste (ESM Figure A-9) until shiny (Figure 17a). We also polished the rear of the block with the same tool and paste (Figure 17b) to compare its specular spectral reflectance to that of a mirror standard (curves E and B in Figure 11).

We imaged the front and rear of the aluminum block, and the mirror standard, in the simple goniometer (Figure 18). It was hard to see retroreflection of the 405-nm violet laser beam from the polished grooves, possibly because at this wavelength the specular near-normal hemispherical reflectance of the polished block (as gauged by that of its rear) is about 0.31, making its two-bounce reflectance only $0.31^2 = 0.096$.

The simple goniometer permits comparative assessment of retroreflection by examining the brightness of light reflected towards the pinhole source. For flat surfaces, this assessment is more relevant at high incidence angles. The results from the mirror calibration standard (top row of Figure 18) provide an example of what we would see with a purely specular and non-retroreflective surface. The results from the hand-polished flat aluminum surface provide an example of what we would see with a non-retroreflective surface that reflects both specularly and diffusely. With these two samples for comparison, we interpret the hand-polished retroreflector prototype's more pronounced light intensities around the pinhole source at incidence angles greater than 50° to be evidence of some retroreflection (bottom row of Figure 18). Ultimately, however, the prototype reflects light at a wide range of angles over a wide range of incidence angles, so its performance in its current state is rather poor.

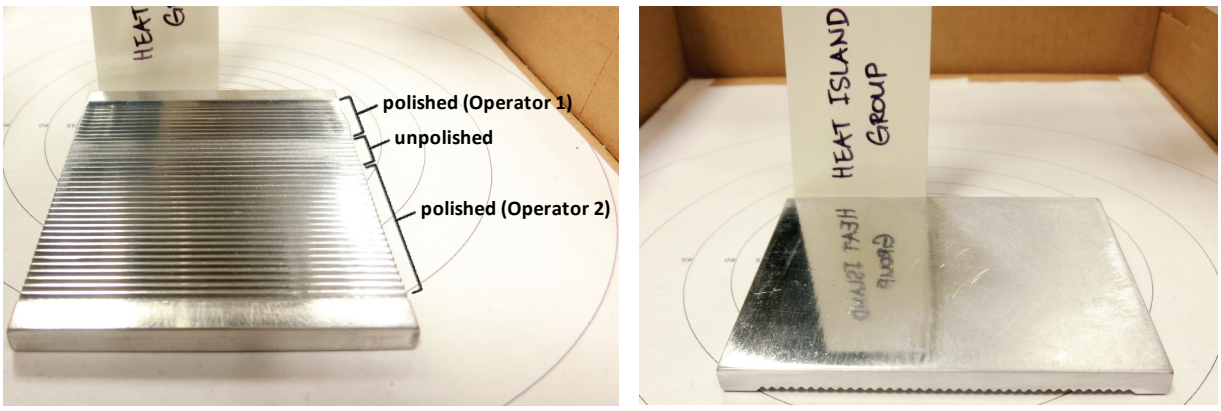

(a) (b)

Figure 17. Polished right-angle groove aluminum block, showing sections of the groove face polished by two different operators (a) and the back face smoothed by one of the operators (b).

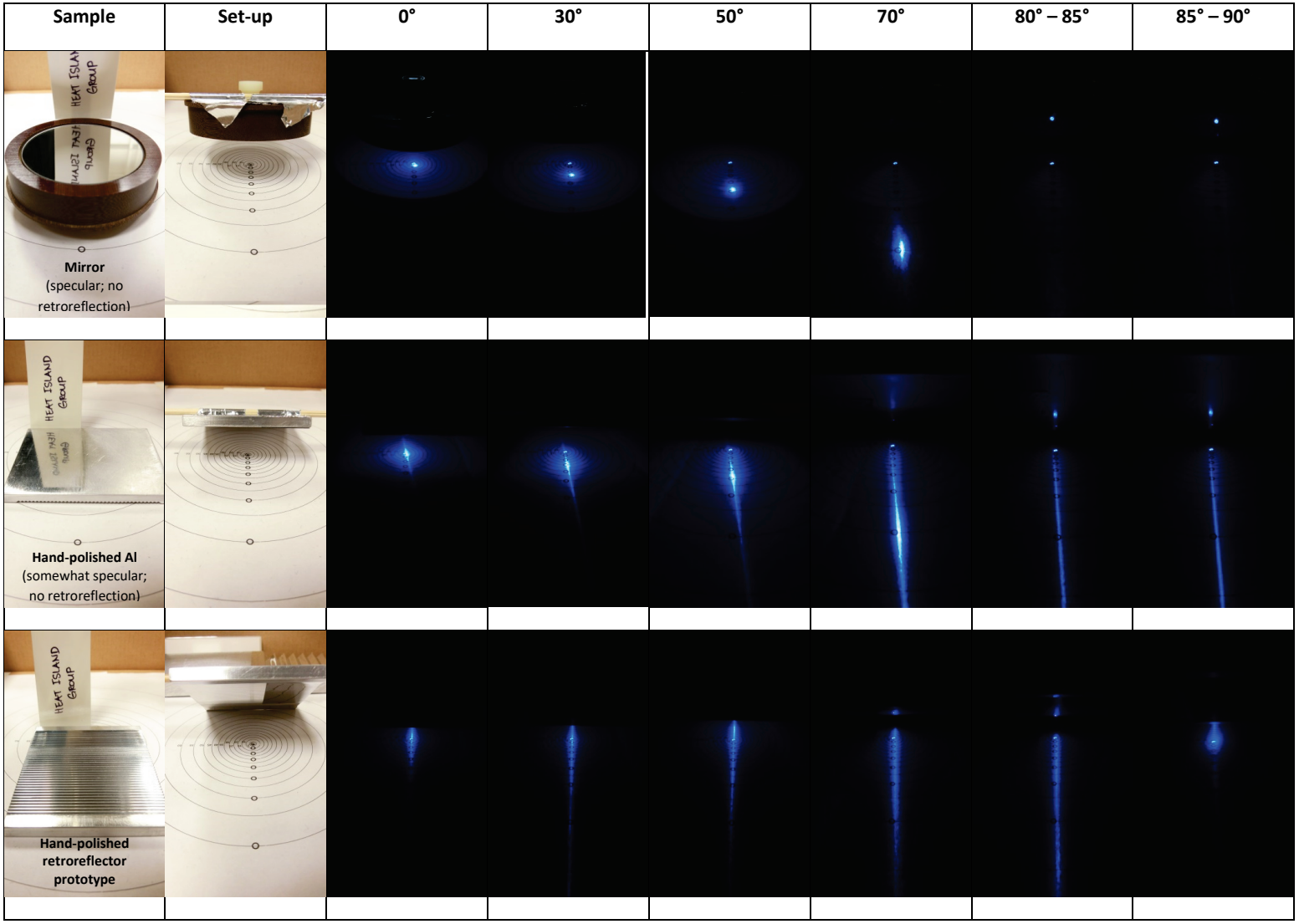

Figure 18. Reflections from three metal surfaces—a mirror reflectance standard, top row; the hand-polished rear face of the aluminum block, middle row; and the hand-polished grooved face of the aluminum block, bottom row—imaged with a violet (405 nm) laser incident at angles of 0 to nearly 90° in the simple goniometer.

6.3 Aluminized Mylar film

Aluminized Mylar film (biaxially oriented polyethylene terephthalate with an aluminum coating) has very high specular reflectance across the solar spectrum, with a metal-face specular solar reflectance of about 0.92, and a plastic-face specular solar reflectance of about 0.84 (curves A and C in Figure 11). With the metal face forward, the two-bounce albedo could be $0.92^2 = 0.83$; with the plastic face forward, it could be $0.83^2 = 0.69$. The aluminized Mylar is nearly opaque to sunlight, with a solar transmittance less than 0.01.

The film's metal and plastic faces have thermal emittances 0.04 and 0.72, respectively, as measured with a Devices & Services Emissometer Model AE1 following ASTM C1371-15: Standard Test Method for Determination of Emittance of Materials Near Room Temperature Using Portable Emissometers [53]. The primary challenges appear to be forming orthogonal folds in the film and keeping the film surfaces flat. We experimented with various methods of creating orthogonal folds in sheets of aluminized Mylar film (thickness 50 μm), including creasing the film, stamping the film in a die, and even adhering it to various shaped or shapeable substrates.

6.3.1 Forming folds in Mylar film

We had difficulties plastically deforming the Mylar sheeting into the desired geometry. Initial attempts at stamping orthogonal folds into the film using a pair of grooved aluminum die blocks failed to produce any significant deformation whatsoever. Manually creasing the film, section by section, did yield permanent folds, but the angles were acute (< 90°) rather than orthogonal (90°). We abandoned this method after limited trials, seeing no simple path forward.

6.3.2 Adhering Mylar film to a grooved substrate

We next tried to attach the metallized Mylar film to a substrate that was already machined to the desired grooved geometry. A recurring challenge was preserving the smooth surfaces and sharp angles of the substrate through the adhesion process. Double-sided tape, for example, allowed the film to bond smoothly to the flat faces of the grooves but could not preserve the sharpness of the 90° peaks and valleys due to the added thickness (Figure 19). We experimented with several types of spray glue, which could be applied in thinner layers, but they tended to deposit as an array of large droplets that formed millimeter-sized bumps underneath the Mylar film. Finally, none of the tested adhesives permitted repositioning after first contact, preventing the use of a stamping press for the adhesion step. Instead, we had to join film to substrate manually, which proved to be an extremely tedious process (ESM Figure A-10). Though we did not further investigate this method, there likely exist other adhesive options (for example, liquids) meriting experimentation.

6.3.3 Forming folds in a two-layer system

We came closest to success using a two-step process in which the Mylar film is first attached to a flat and ductile substrate and the two-layer system is subsequently shaped. We experimented with adhesive-

backed aluminum foil as the ductile substrate. There were no significant difficulties adhering flat sheets of Mylar film and aluminum foil, and we found the resultant two-layer system to be amenable to shaping via many methods, including stamping in a die (Figure 20) and bending in corrugators of varying design (ESM Figure A-11). A paper corrugator with sharp and narrow gear teeth, for example, produced 4-mm pitch rounded folds with slight inconsistencies in size, and a paint-tube wringer with short and blunt gear teeth produced consistent 3-mm pitch rounded folds (ESM Figure A-12). Corrugation was the fastest and simplest shaping method tested, but we acknowledge that the resulting rounded fold profiles need further adjustment to achieve the desired sharp 90° angle fold geometry (Figure 21).

6.3.4 Additional challenges and next steps

We note at least two additional areas for improvement: (1) the methods we explored and described previously did not readily scale down to grooved geometries of smaller pitch size (say, less than 3 mm); and (2) all methods produced some degree of undesirable scratch marks on the highly-reflective and fragile bare metal side of the film.

We will measure the bi-directional reflectivities of an orthogonally folded Mylar film in future work after we have demonstrated a satisfactory folding technique.

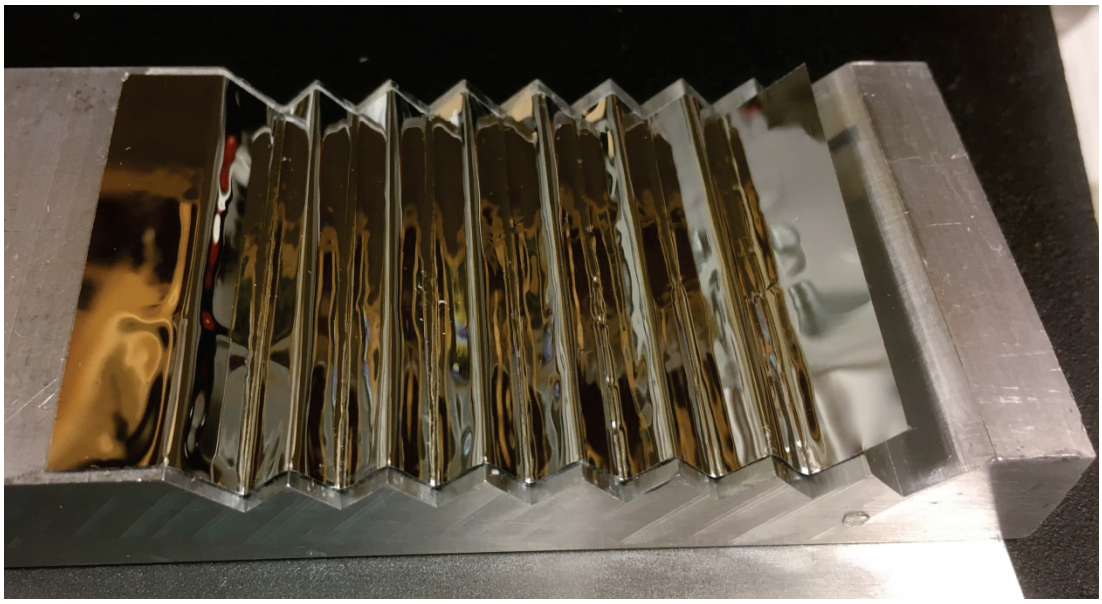

Figure 19. Aluminized Mylar adhered with double-sided tape to a pre-shaped aluminum block with 7-mm pitch orthogonal grooves. With this method, the groove faces are decently smooth, but the added thickness from the layer of tape makes it difficult to conform to the sharp edges of the grooves.

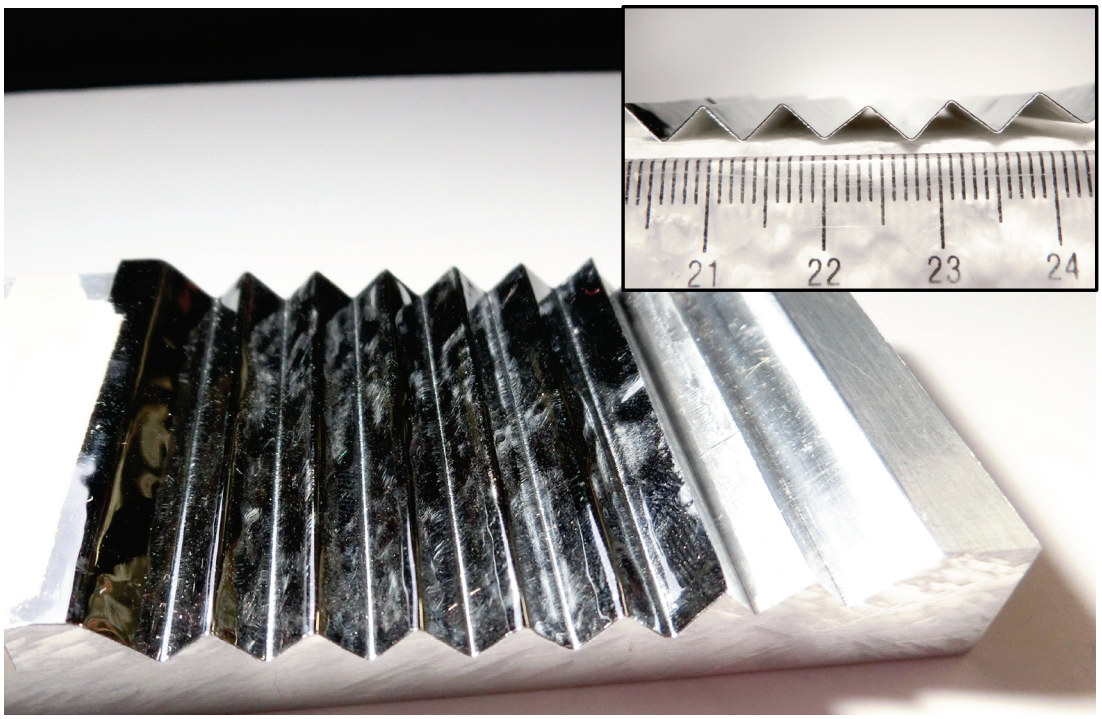

Figure 20. A two-layer sheet consisting of aluminized Mylar adhered to aluminum foil tape is shaped using the same 7-mm pitch grooved aluminum block as a die. This two-layer system readily conforms to the shape of the grooved mold, but substantial scratches can be seen on the delicate bare metal side of the film.

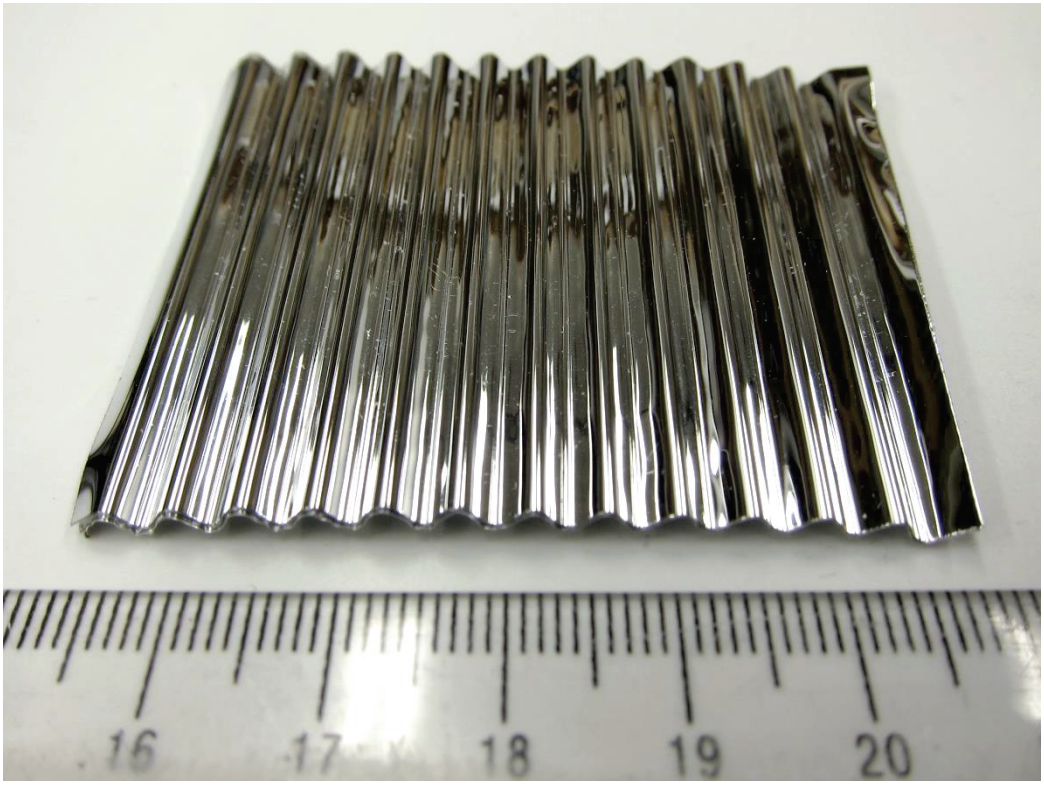

(a)

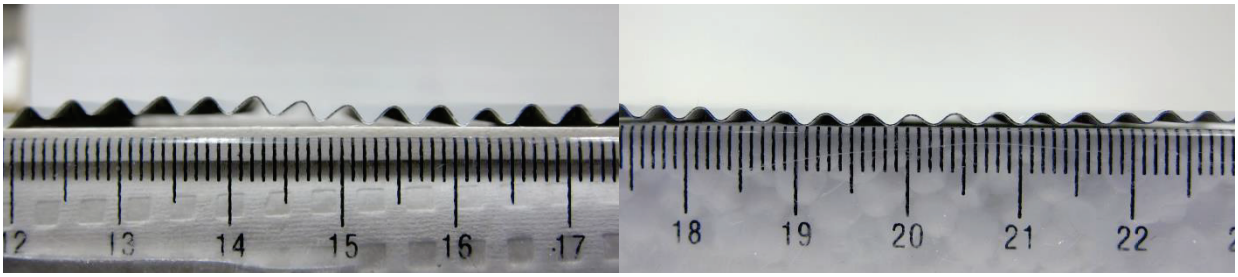

(b) (c)

Figure 21. Feeding the Mylar-on-foil two-layer sheet through corrugators proved a fast and simple method of producing repeating bends, but the resultant folds are rounded instead of the desired sharp 90° angles (a). Different corrugators produced slightly different fold profiles. In panel *b*, the fold profile produced by a paper corrugator; in panel *c*, the fold profile produced by a tube wringer.

7 Summary

Raising urban albedo increases the fraction of incident sunlight returned to outer space, cooling cities and their buildings. Retroreflective cool walls could improve upon diffusely reflecting cool walls by reflecting incoming beam radiation to the solar disc (if the retroreflection is three dimensional and ideal) or at least upwards (if the retroreflection is two dimensional and/or imperfect). For example, a retroreflective wall

with albedo 0.60 could reflect 55% of incident sunlight to the sky, while a Lambertian wall of the same albedo would reflect only 36% of this light skyward.

The greatest challenge in retroreflective wall design appears to be the need to operate at large incidence angles to reflect a substantial portion of incident sunlight. First-principle physics and ray-tracing simulations suggest that it will be difficult to achieve this with surfaces that rely on total internal reflection; this appears to be confirmed by solar spectral bi-directional reflectivity measurements made on a prismatic bicycle reflector, and seemingly (though not conclusively) corroborated by comparison in a simple goniometer of the intensities of the Fresnel and retro reflections from commercial glass bead and prismatic retroreflective safety films. The modest retroreflection from these films observed in the simple goniometer at large incidence angles (50–70°) suggests that they may not be ideal materials for retroreflective cool wall, but further quantitative evaluation is merited.

Initial efforts focused on evaluating the suitability of two categories of commercial retroreflective materials, prismatic bicycle retroreflectors and traffic safety films, for potential use in retroreflective cool wall applications. Two instruments used in the characterization of retroreflective performance were a gonio-spectrophotometer that quantifies solar spectral bi-directional reflectivity, and a simple goniometer that generates images of reflection patterns. Gonio-spectrophotometer measurements showed bicycle retroreflectors to have poor retroreflectance at large incidence angles, and simple goniometer measurements of four different types of white traffic safety films using violet (405 nm) and green (532 nm) lasers suggested retroreflectance limits of 0.09 at incidence angles up to 45°, and 0.30 at incidence angles of up to 70°.

Attempts to produce a two-surface retroreflector with orthogonal mirror grooves by cutting and polishing an aluminum block indicate that residual surface roughness impedes retroreflection. Ongoing efforts focus on shaping aluminized Mylar film, a material with very high specular reflectance across the solar spectrum. We investigated three methods of imparting orthogonally grooved geometry on a sheet of aluminized Mylar film: (1) folding the film or stamping it in a die; (2) adhering the film to a pre-shaped substrate; and (3) using a two-step process where the film is first attached to a flat ductile substrate, then bent or stamped into the desired grooved shape. The latter two techniques were most successful in our trials, but we continue to seek an efficient, scalable, and non-destructive method.

Acknowledgements

This research was supported by the California Energy Commission under contract EPC-14-010, and by the Assistant Secretary for Energy Efficiency and Renewable Energy, Building Technologies Office of the U.S. Department of Energy under Contract No. DE-AC02-05CH11231. We wish to thank Pablo Rosado of LBNL for use of ESM Figure A-3.

References

[1] M. Santamouris, Cooling the cities - A review of reflective and green roof mitigation technologies to fight heat island and improve comfort in urban environments, Sol. Energy. 103 (2014) 682–703.

doi:10.1016/j.solener.2012.07.003.

[2] J. Zhang, A. Mohegh, Y. Li, R. Levinson, G. Ban-Weiss, Systematic comparison of the influence of cool wall versus cool roof adoption on urban climate in the Los Angeles basin, Environ. Sci. Technol. 52 (2018) 11188–11197. doi:10.1021/acs.est.8b00732.

[3] H. Akbari, S. Menon, A. Rosenfeld, Global cooling: Increasing world-wide urban albedos to offset CO2, Clim. Change. 94 (2009) 275–286. doi:10.1007/s10584-008-9515-9.

[4] H. Akbari, H.D. Matthews, Global cooling updates: Reflective roofs and pavements, Energy Build. 55 (2012) 2–6. doi:10.1016/j.enbuild.2012.02.055.

[5] H. Akbari, H. Damon Matthews, D. Seto, The long-term effect of increasing the albedo of urban areas, Environ. Res. Lett. (2012). doi:10.1088/1748-9326/7/2/024004.

[6] J. Zhang, K. Zhang, J. Liu, G. Ban-Weiss, Revisiting the climate impacts of cool roofs around the globe using an Earth system model, Environ. Res. Lett. (2016). doi:10.1088/1748-9326/11/8/084014.

[7] D. Millstein, S. Menon, Regional climate consequences of large-scale cool roof and photovoltaic array deployment, Environ. Res. Lett. 6 (2011). doi:10.1088/1748-9326/6/3/034001.

[8] A. Mohegh, P. Rosado, L. Jin, D. Millstein, R. Levinson, G. Ban-Weiss, Modeling the climate impacts of deploying solar reflective cool pavements in California cities, J. Geophys. Res. 122 (2017) 6798–6817. doi:10.1002/2017JD026845.

[9] A. Mohegh, R. Levinson, H. Taha, H. Gilbert, J. Zhang, Y. Li, T. Tang, G. Ban-Weiss, Observational evidence of neighborhood scale reductions in air temperature associated with increases in roof albedo, Climate. 6 (2018) 98. doi:10.3390/cli6040098.

[10] H.E. Gilbert, P.J. Rosado, G. Ban-Weiss, J.T. Harvey, H. Li, B.H. Mandel, D. Millstein, A. Mohegh, A. Saboori, R.M. Levinson, Energy and environmental consequences of a cool pavement campaign, Energy Build. 157 (2017) 53–77. doi:10.1016/j.enbuild.2017.03.051.

[11] H. Taha, H. Akbari, A. Rosenfeld, J. Huang, Residential cooling loads and the urban heat island—the effects of albedo, Build. Environ. 23 (1988) 271–283. doi:10.1016/0360-1323(88)90033-9.

[12] R. Levinson, H. Akbari, Potential benefits of cool roofs on commercial buildings: Conserving energy, saving money, and reducing emission of greenhouse gases and air pollutants, Energy Effic. 3 (2010) 53–109. doi:10.1007/s12053-008-9038-2.

[13] P.J. Rosado, R. Levinson, Potential benefits of cool walls on residential and commercial buildings across California and the United States: conserving energy, saving money, and reducing emission of greenhouse gases and air pollutants, Energy Build. 199 (2019) 1–20. doi:10.1016/j.enbuild.2019.02.028.

[14] P.J. Rosado, G. Ban-Weiss, A. Mohegh, R.M. Levinson, Influence of street setbacks on solar reflection and air cooling by reflective streets in urban canyons, Sol. Energy. 144 (2017) 144–157. doi:10.1016/j.solener.2016.12.026.

[15] R. Levinson, Using solar availability factors to adjust cool-wall energy savings for shading and reflection by neighboring buildings, Sol. Energy. 180 (2019) 717–734. doi:10.1016/j.solener.2019.01.023.

[16] J. Yuan, K. Emura, C. Farnham, Potential for application of retroreflective materials instead of highly reflective materials for urban heat island mitigation, Urban Stud. Res. 2016 (2016) 1–10. doi:10.1155/2016/3626294.

[17] Y. Qin, J. Liang, K. Tan, F. Li, A side by side comparison of the cooling effect of building blocks with retro-reflective and diffuse-reflective walls, Sol. Energy. 133 (2016) 172–179. doi:10.1016/j.solener.2016.03.067.

[18] F. Rossi, E. Morini, B. Castellani, A. Nicolini, E. Bonamente, E. Anderini, F. Cotana, Beneficial effects of retroreflective materials in urban canyons: Results from seasonal monitoring campaign, J. Phys. Conf. Ser. 655 (2015). doi:10.1088/1742-6596/655/1/012012.

[19] F. Rossi, B. Castellani, A. Presciutti, E. Morini, E. Anderini, M. Filipponi, A. Nicolini, Experimental evaluation of urban heat island mitigation potential of retro-reflective pavement in urban canyons, Energy Build. 126 (2016) 340–352. doi:10.1016/j.enbuild.2016.05.036.

[20] H. Iyota, H. Sakai, K. Emura, Method for measuring solar reflectance of retroreflective materials using emitting-receiving optical fiber, in: Second Int. Conf. Countermeas. To Urban Heat Islands, Berkeley, California (21 - 23 September), 2009. https://heatisland.lbl.gov/sites/default/files/cuhi/docs/211510-iyota-doc.pdf.

[21] J. Yuan, K. Emura, C. Farnham, H. Sakai, Application of glass beads as retro-reflective facades for urban heat island mitigation: Experimental investigation and simulation analysis, Build. Environ. 105 (2016) 140–152. doi:10.1016/j.buildenv.2016.05.039.

[22] J. Yuan, K. Emura, H. Sakai, C. Farnham, S. Lu, Optical analysis of glass bead retro-reflective materials for urban heat island mitigation, Sol. Energy. 132 (2016) 203–213. doi:10.1016/j.solener.2016.03.011.

[23] F. Rossi, A.L. Pisello, A. Nicolini, M. Filipponi, M. Palombo, Analysis of retro-reflective surfaces for urban heat island mitigation: A new analytical model, Appl. Energy. 114 (2014) 621–631. doi:10.1016/j.apenergy.2013.10.038.

[24] F. Rossi, B. Castellani, A. Presciutti, E. Morini, M. Filipponi, A. Nicolini, M. Santamouris, Retroreflective façades for urban heat island mitigation: Experimental investigation and energy evaluations, Appl. Energy. 145 (2015) 8–20. doi:10.1016/j.apenergy.2015.01.129.

[25] B. Castellani, E. Morini, E. Anderini, M. Filipponi, F. Rossi, Development and characterization of retro-reflective colored tiles for advanced building skins, Energy Build. 154 (2017) 513–522. doi:10.1016/j.enbuild.2017.08.078.

[26] T. Harima, T. Nagahama, Evaluation methods for retroreflectors and quantitative analysis of near-infrared upward reflective solar control window film—Part II: Optical properties evaluation and verification results, Sol. Energy. 148 (2017) 164–176. doi:10.1016/j.solener.2017.03.025.

[27] T. Harima, T. Nagahama, Evaluation methods for retroreflectors and quantitative analysis of near-infrared upward reflective solar control window film—Part I: Theory and evaluation methods, Sol. Energy. 148 (2017) 177–192. doi:10.1016/j.solener.2017.02.016.

[28] M. Ichinose, T. Inoue, T. Nagahama, Effect of retro-reflecting transparent window on anthropogenic urban heat balance, Energy Build. (2017). doi:10.1016/j.enbuild.2017.01.051.

[29] E. Morini, B. Castellani, A. Presciutti, M. Filipponi, A. Nicolini, F. Rossi, Optic-energy performance improvement of exterior paints for buildings, Energy Build. 139 (2017) 690–701. doi:10.1016/j.enbuild.2017.01.060.

[30] E. Morini, B. Castellani, E. Anderini, A. Presciutti, A. Nicolini, F. Rossi, Optimized retro-reflective tiles for exterior building element, Sustain. Cities Soc. 37 (2018) 146–153. doi:10.1016/j.scs.2017.11.007.

[31] L. Mauri, G. Battista, E. de Lieto Vollaro, R. de Lieto Vollaro, Retroreflective materials for building's façades: Experimental characterization and numerical simulations, Sol. Energy. 171 (2018) 150–156. doi:10.1016/j.solener.2018.06.073.

[32] H. Sakai, K. Emura, N. Igawa, H. Iyota, Reduction of reflected heat of the sun by retroreflective materials, in: Second Int. Conf. Countermeas. To Urban Heat Islands, Berkeley, California (21 - 23 September), 2009. https://heatisland.lbl.gov/sites/default/files/cuhi/docs/211450-sakai-doc.pdf.

[33] J. Yuan, K. Emura, C. Farnham, A method to measure retro-reflectance and durability of retro-reflective materials for building outer walls, J. Build. Phys. 38 (2015) 500–516. doi:10.1177/1744259113517208.

[34] J. Yuan, C. Farnham, K. Emura, A study on the accuracy of determining the retro-reflectance of retro-reflective material by heat balance, Sol. Energy. 122 (2015) 419–428. doi:10.1016/j.solener.2015.08.040.

[35] R. Levinson, S. Chen, C. Ferrari, P. Berdahl, J. Slack, Methods and instrumentation to measure the effective solar reflectance of fluorescent cool surfaces, Energy Build. 152 (2017) 752–765. doi:10.1016/j.enbuild.2016.11.007.

[36] ASTM International, ASTM D4596-17: Standard Specification for Retroreflective Sheeting for Traffic Control, West Conshohocken, PA, 2017. doi:10.1520/D4956-17.

[37] X. Meng, T. Luo, Z. Wang, W. Zhang, B. Yan, J. Ouyang, E. Long, Effect of retro-reflective materials on building indoor temperature conditions and heat flow analysis for walls, Energy Build. 127 (2016) 488–498. doi:10.1016/j.enbuild.2016.05.094.

[38] J. Yuan, C. Farnham, K. Emura, Development of a retro-reflective material as building coating and evaluation on albedo of urban canyons and building heat loads, Energy Build. 103 (2015) 107–117. doi:10.1016/j.enbuild.2015.06.055.

[39] J. Yuan, K. Emura, C. Farnham, Geometrical-optics analysis of reflective glass beads applied to building coatings, Sol. Energy. 122 (2015) 997–1010. doi:10.1016/j.solener.2015.10.015.

[40] J. Yuan, K. Emura, C. Farnham, A study on the durability of a glass bead retro-reflective material applied to building facades, Prog. Org. Coatings. 120 (2018) 36–48. doi:10.1016/j.porgcoat.2018.03.009.

[41] H. Sakai, H. Iyota, Development of two new types of retroreflective materials as countermeasures to urban heat islands, Int. J. Thermophys. 38 (2017) 1–10. doi:10.1007/s10765-017-2266-y.

[42] R. Levinson, H. Akbari, P. Berdahl, Measuring solar reflectance—Part I: Defining a metric that accurately predicts solar heat gain, Sol. Energy. 84 (2010) 1717–1744. doi:10.1016/j.solener.2010.04.018.

[43] J.A. Duffie, W.A. Beckman, Solar Engineering of Thermal Processes, 3rd ed., Wiley, 2006.

[44] National Renewable Energy Laboratory, National Solar Radiation Data Base, 1991- 2005 Update: Typical Meteorological Year 3, (2018). http://rredc.nrel.gov/solar/old_data/nsrdb/1991-2005/tmy3.

[45] National Renewable Energy Laboratory, Measurement and Information Data Center Solar Position and Intensity (MIDC SOLPOS) Calculator, (2018). https://midcdmz.nrel.gov/solpos/solpos.html.

[46] R. Tu, Ray Optics Simulation web application, (2018). http://ricktu288.github.io/ray-optics.

[47] ASTM International, ASTM E903-12: Standard Test Method for Solar Absorptance, Reflectance,

and Transmittance of Materials Using Integrating Spheres, West Conshohocken, PA, 2012. doi:10.1520/E0903-12.

[48] R. Levinson, AM1GH solar spectral irradiance, (2018). http://coolcolors.lbl.gov/irradiance.

[49] Georgia State University, Hyperphysics tutorial: Fresnel's equations, (2018). http://hyperphysics.phy-astr.gsu.edu/hbase/phyopt/freseq.html#c1.

[50] ASTM International, ASTM D4280-18: Standard Specification for Extended Life Type, Nonplowable, Raised Retroreflective Pavement Markers, West Conshohocken, PA, 2018. doi:10.1520/D4280-18.

[51] M.N. Polyanskiy, Refractive index database, (2018). http://refractiveindex.info.

[52] International Organization for Standardization, ISO 9050:2003: Glass in building—Determination of light transmittance, solar direct transmittance, total solar energy transmittance, ultraviolet transmittance and related glazing factors, 2003. https://www.iso.org/standard/35062.html.

[53] ASTM International, ASTM C1371-15: Standard Test Method for Determination of Emittance of Materials Near Room Temperature Using Portable Emissometers, West Conshohocken, PA, 2015. doi:10.1520/C1371-15.

Appendix A: Electronic Supplementary Material

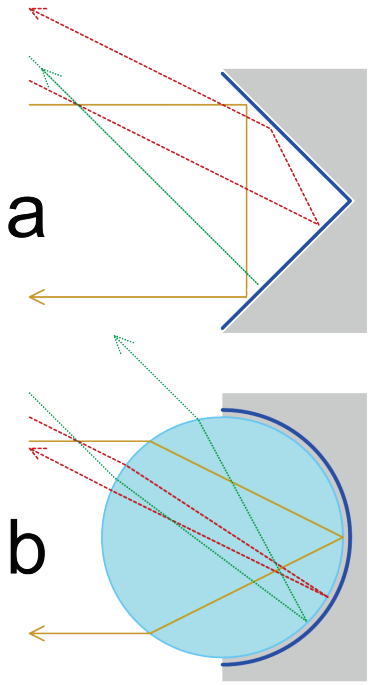

ESM Figure A-1. Light reflection from (a) corner and (b) spherical retroreflectors. Adapted from Cmglee[1].

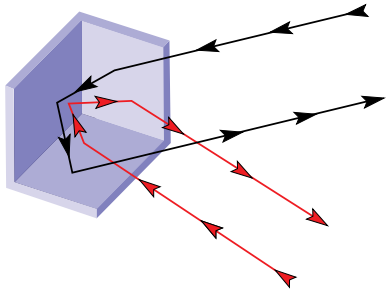

ESM Figure A-2. Three-surface corner retroreflector returning light incident from any direction to its source. Source: Chetvorno[2].

---

[1] Cmglee, Comparison of retroreflectors (used under Creative Commons license; https://creativecommons.org/licenses/by-sa/3.0/legalcode), (2018). https://commons.wikimedia.org/wiki/File:Comparison_of_retroreflectors.svg.

[2] Chetvorno, Corner retroreflector (public domain image), (2018). https://en.wikipedia.org/wiki/Retroreflector#/media/File:Corner_reflector.svg.

CZ: City, State
1A: Miami, FL
2A: Houston, TX
2B: Phoenix, AZ
3A: Memphis, TN
3B: El Paso, TX
BU: Burbank, CA
FR: Fresno, CA
3C: San Francisco, CA
4A: Baltimore, MD
4B: Albuquerque, NM
4C: Seattle, WA
5A: Chicago, IL
5B: Boise, ID
6A: Burlington, VT
6B: Helena, MT
7: Duluth, MN
8: Fairbanks, AK

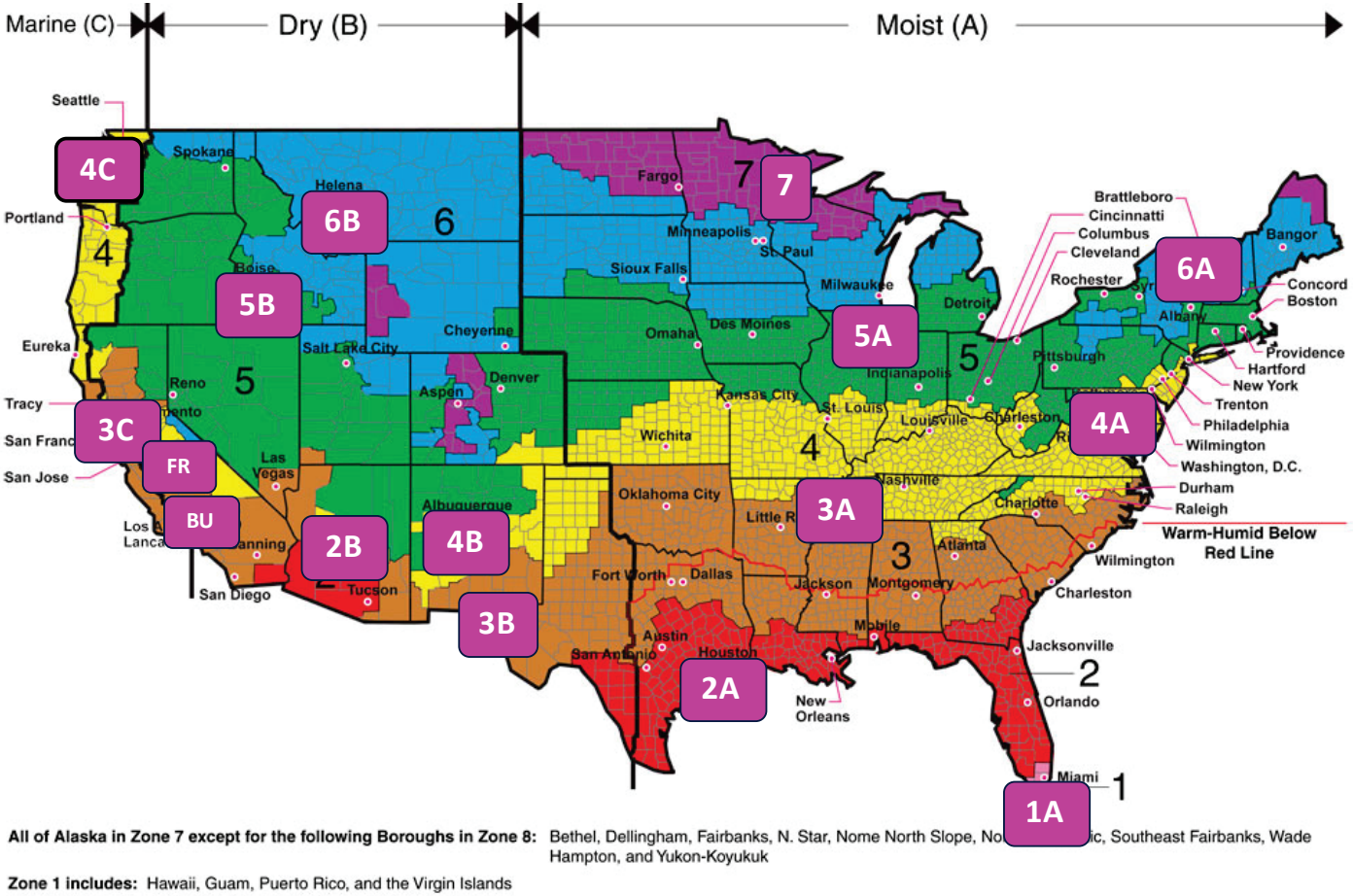

ESM Figure A-3. Map of U.S cities representing ASHRAE climate zones (CZ) 1 – 8, plus two California cities (Burbank and Fresno). Source: Rosado et al. [13].

ESM Table A-1. Percentage of beam sunlight incident on an isolated north, east, south, or west wall in summer at solar altitude angles up to 5, 15, 30, 45, 60, or 75°, reported for the climates shown in ESM Figure A-3.

	(a) north						(b) east						(c) south						(d) west					
Climate	**5°**	**15°**	**30°**	**45°**	**60°**	**75°**	**5°**	**15°**	**30°**	**45°**	**60°**	**75°**	**5°**	**15°**	**30°**	**45°**	**60°**	**75°**	**5°**	**15°**	**30°**	**45°**	**60°**	**75°**
1A	0	22	62	88	99	100	0	9	30	54	78	95	0	0	1	6	27	73	1	4	22	49	73	97
2A	5	37	78	98	100	100	2	10	32	56	82	97	0	0	1	7	30	80	0	9	31	53	79	99
2B	30	60	90	100	100	100	6	18	37	62	84	100	0	0	0	10	32	90	6	15	36	60	82	100
3A	9	34	81	100	100	100	2	9	33	63	85	98	0	0	1	9	40	86	2	9	31	65	86	98
3B	3	28	82	99	100	100	1	8	40	62	83	97	0	0	1	7	30	80	1	9	28	61	85	98
BU	8	26	84	100	100	100	2	9	34	65	85	98	0	0	1	8	36	85	2	5	33	62	84	97
FR	10	42	85	100	100	100	3	12	37	67	87	99	0	0	1	10	41	95	3	12	35	69	87	99
3C	23	51	94	100	100	100	3	9	35	59	84	100	0	0	1	10	42	97	5	13	33	63	89	100
4A	21	51	93	100	100	100	1	8	36	64	87	100	0	0	1	11	45	100	6	15	35	70	88	100
4B	17	45	92	100	100	100	6	15	45	65	86	98	0	0	1	7	35	86	3	12	31	61	85	98
4C	28	71	99	100	100	100	3	13	37	68	96	100	0	0	2	20	74	100	4	16	40	75	94	100
5A	11	48	92	100	100	100	2	11	36	70	90	100	0	0	1	15	52	100	1	9	36	67	88	100
5B	17	59	100	100	100	100	4	16	41	69	93	100	0	0	2	16	62	100	3	13	46	70	92	100
6A	35	68	97	100	100	100	5	15	39	73	92	100	0	0	2	19	64	100	7	17	41	73	92	100
6B	16	55	100	100	100	100	3	15	45	71	96	100	0	0	2	18	71	100	3	12	44	69	96	100
7	22	67	99	100	100	100	2	14	42	70	96	100	0	0	2	20	72	100	4	17	39	75	94	100
8	50	89	100	100	100	100	14	38	69	97	100	100	0	0	12	77	100	100	1	7	51	93	100	100

ESM Table A-2. Real refractive indices and critical angles of some transparent materials.

Material	Real refractive index	Critical angle in air (°)	Maximum solar altitude angle yielding total internal reflection at face 2 (°)
Low-index glass [a]	1.5	41.8	3.2
High-index glass [b]	2.0	30.0	15.0
Cubic zirconia	2.2	27.0	18.0
Diamond	2.4	24.6	20.4

[a] Such as Schott N-BK7 crown glass [51].

[b] Such as Ohara Glass lanthanum S-LaH79 [51].

ESM Table A-3. Fresnel reflectances of p (parallel)-polarized light (R_p), s (perpendicular)-polarized light (R_s), and unpolarized light ($\bar{R}$) in air striking a surface of real refractive index 1.5 at incidence angle θ.

θ (°)	5	10	15	20	25	30	35	40	45	50	55	60	65	70	75
R_p	0.04	0.04	0.04	0.03	0.03	0.03	0.02	0.01	0.01	0.00	0.00	0.00	0.01	0.04	0.11
R_s	0.04	0.04	0.04	0.05	0.05	0.06	0.07	0.08	0.09	0.11	0.14	0.18	0.23	0.30	0.40
$\bar{R}$	0.04	0.04	0.04	0.04	0.04	0.04	0.04	0.05	0.05	0.06	0.07	0.09	0.12	0.17	0.25

Designed by Ronnen Levinson, Heat Island Group, Lawrence Berkeley National Laboratory (RML27@cornell.edu)

50 mm

Center specimen 20 mm above rings

ESM Figure A-4. Simple goniometer circular grid graphic.

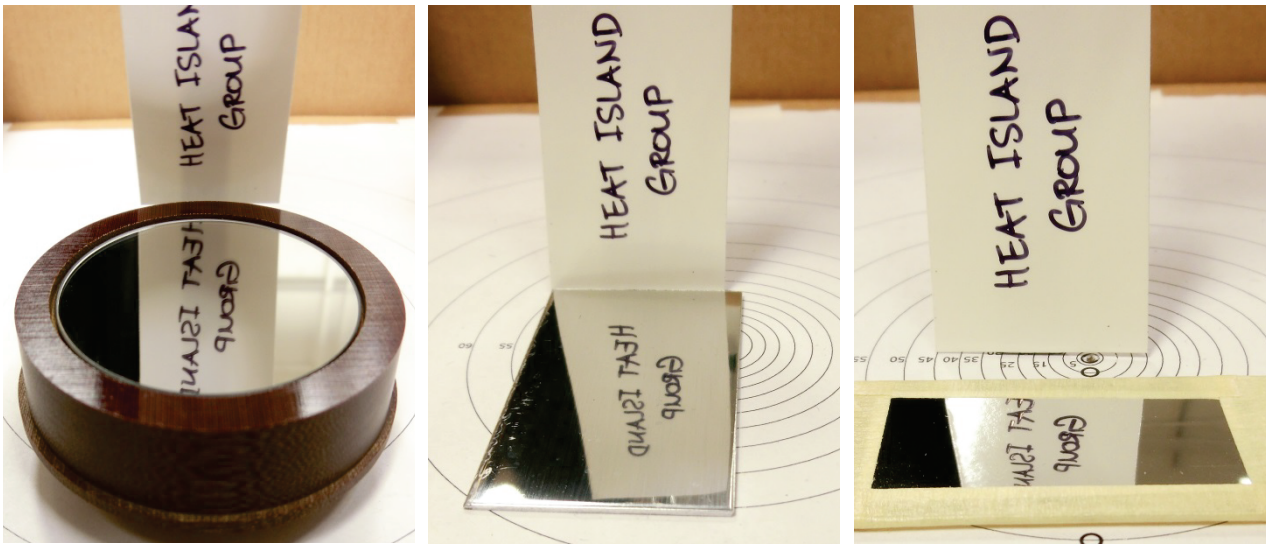

(a) (b) (c)

ESM Figure A-5. Photos of the three non-retroreflective surfaces tested in the simple goniometer. In panel *a*, a mirror calibration standard; in panel *b*, a polished aluminum panel with faint residual grit lines running lengthwise; and in panel *c*, a sheet of aluminized Mylar film (metal face exposed) taped to a flat surface.

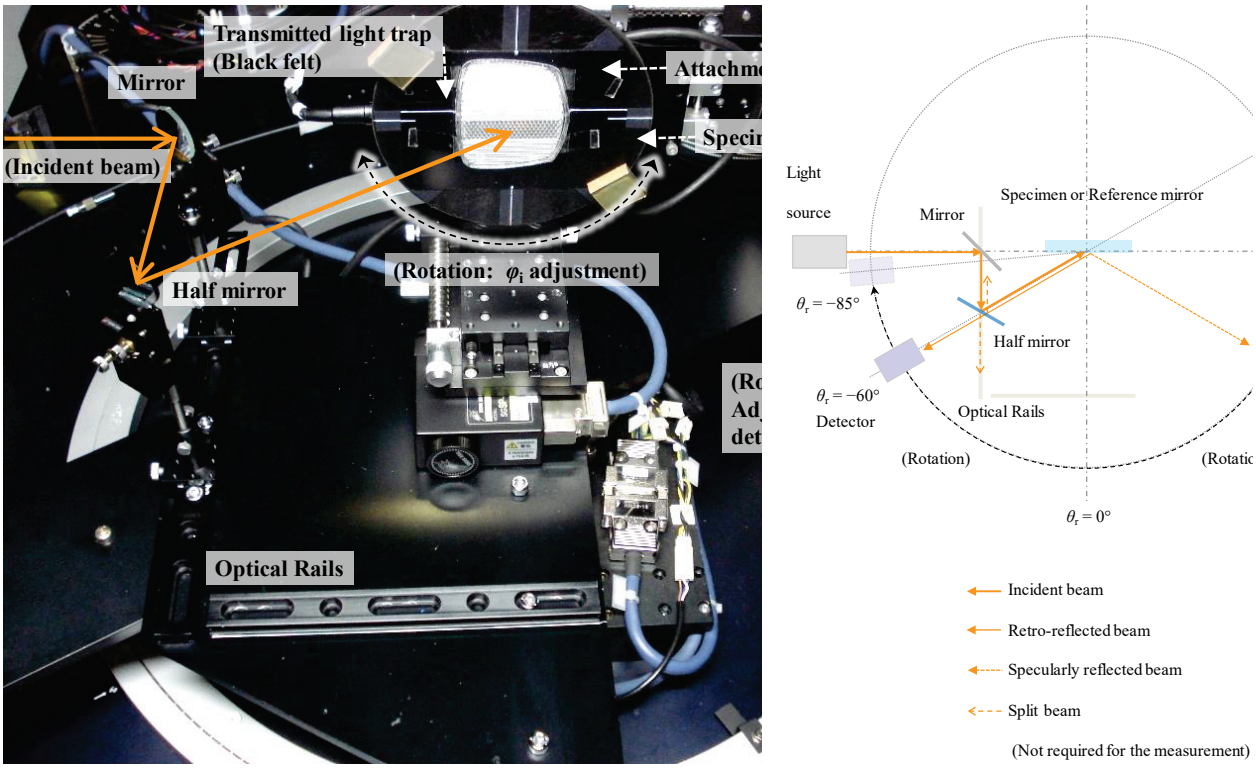

(a) (b)

ESM Figure A-6. Measurement of retroreflectance with Dexerials' gonio-spectrophotometer, showing (a) photo and (b) schematic of bicycle reflector illuminated at incident polar angle of 60° and incident azimuth angle of 0°.

ESM Figure A-7. A close-up view of the simple goniometer turnable rod and specimen holder. Mounted here is a sample of Sheeting C, an ASTM D4956 Type 11 white safety film that exhibits azimuthal sensitivity in retroreflective performance. The sample is oriented with its primary pattern lines (horizontal) running perpendicular to the plane of incidence (that containing incident ray and surface normal).

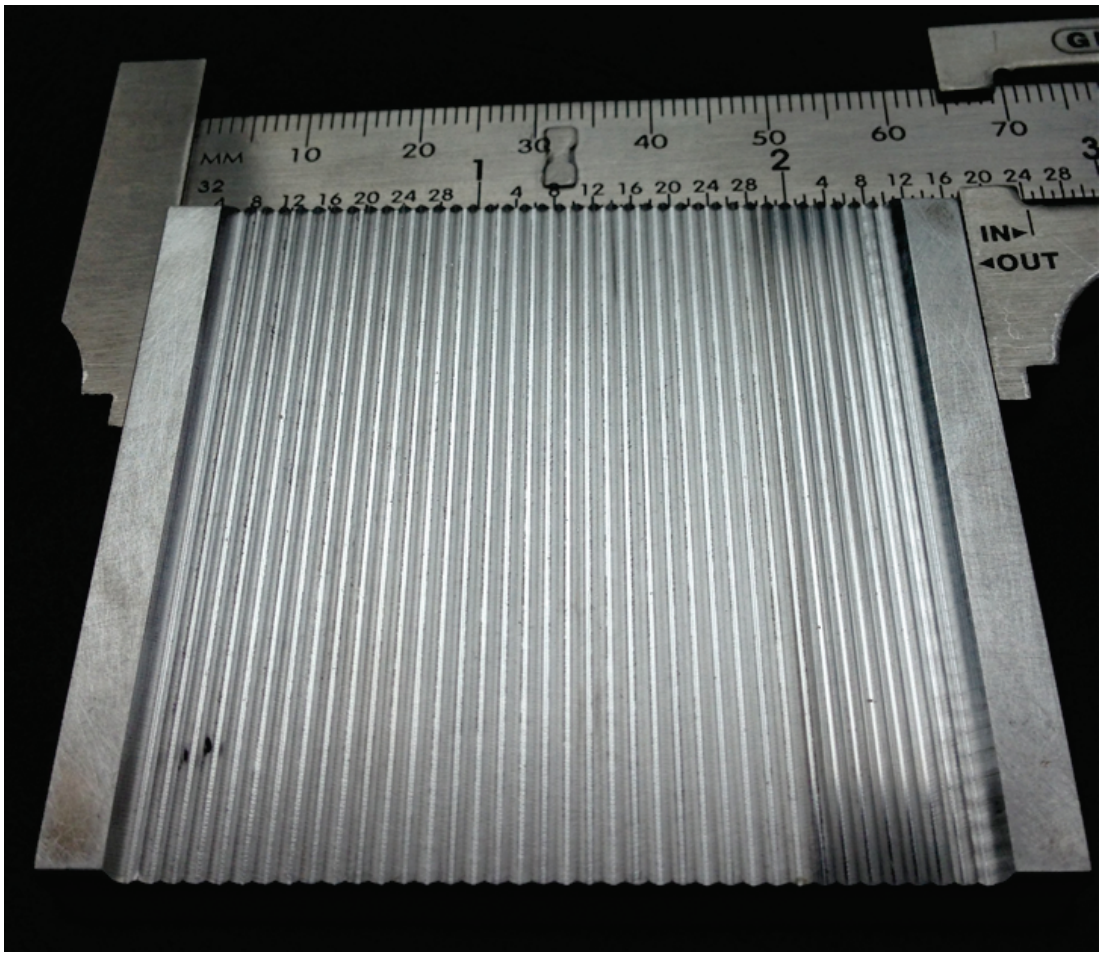

ESM Figure A-8. Unpolished aluminum block with 2-mm pitch orthogonal grooves.

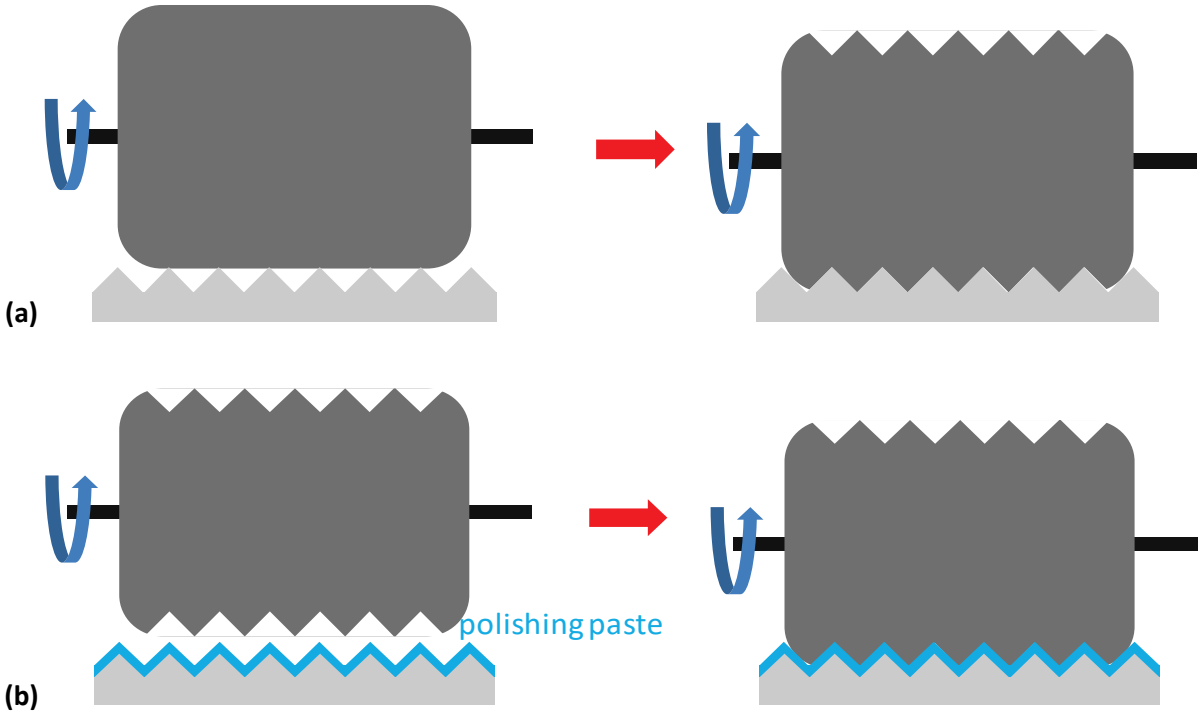

ESM Figure A-9. Polishing of the orthogonally grooved aluminum block, showing (a) initial shaping of the buffing wheel to match the grooved profile of the aluminum block, and (b) subsequent polishing of the groove faces with polishing paste.

(a)

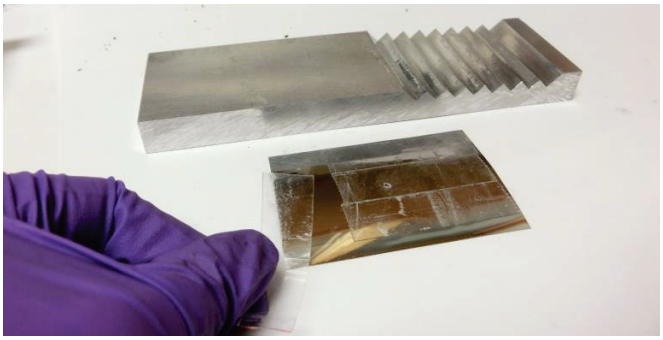

(b)

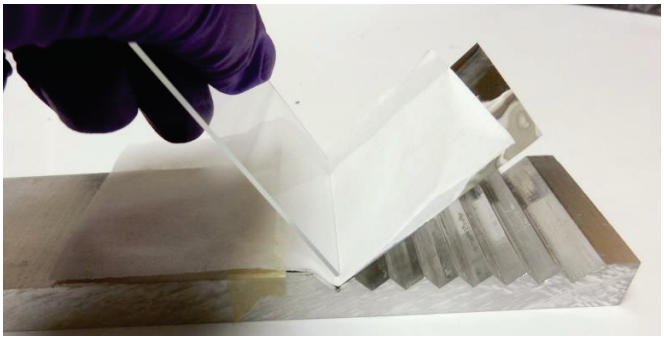

(c)

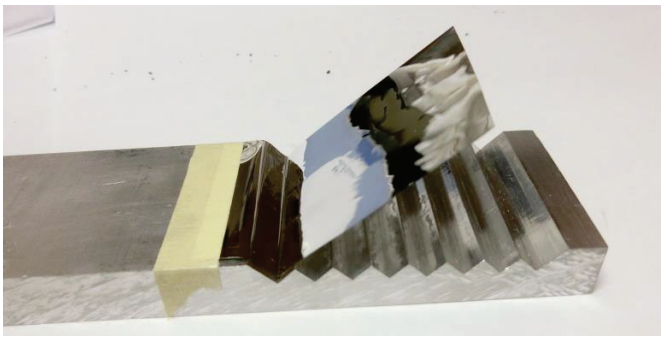

(d)

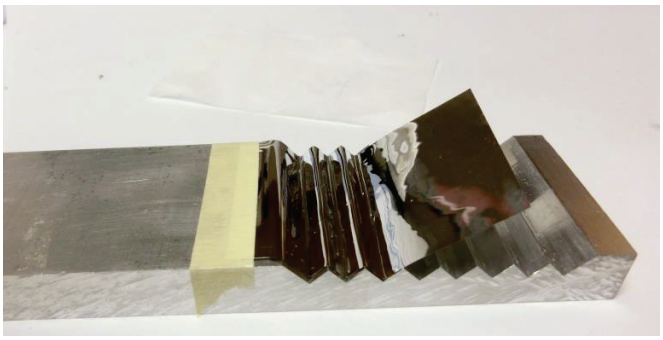

ESM Figure A-10. Manually joining aluminized Mylar film to a grooved aluminum block with double-sided tape. First, the rear face (plastic) of a long pre-cut rectangular piece of the film is lined with double-sided tape (panel *a*). The short edge of the film—with taped side facing the grooved block—is aligned to an end groove, and the film is then pressed firmly against each adjacent groove face, valley, or peak until the entire block has been surfaced (panels *b* through *d*). Although tedious, this sequence of steps is necessary because tape forms a strong bond on initial contact that weakens with subsequent repositioning.

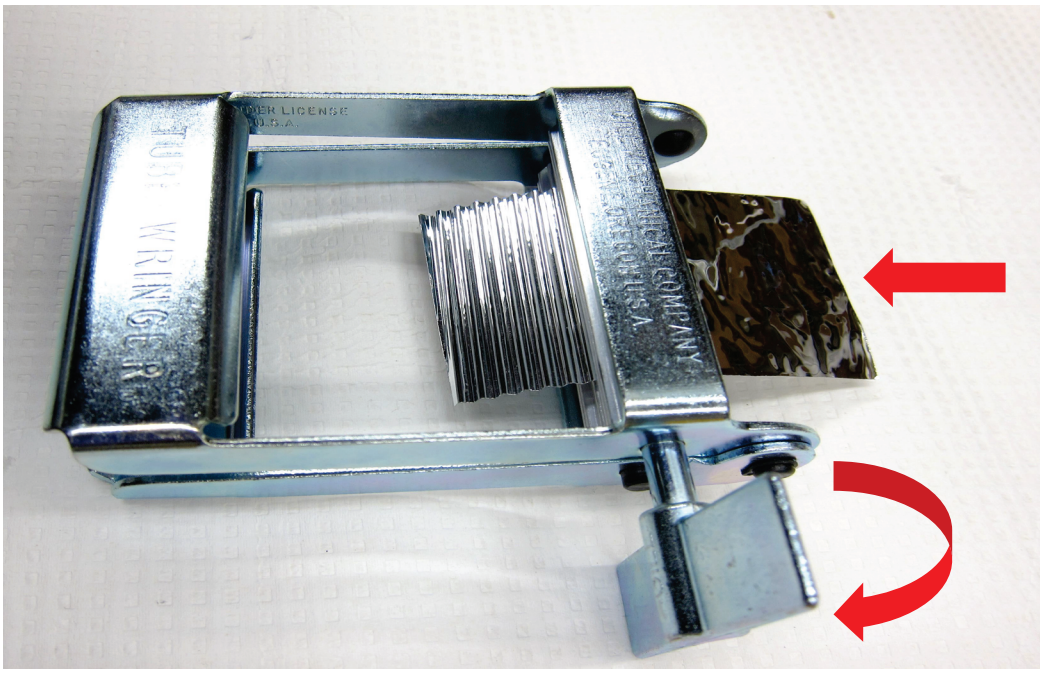

ESM Figure A-11. In a corrugator, a flat sheet is fed through and sequentially bent in opposite directions between two rotating interlocking gears. In our tests, the paint-tube wringer shown above provided a fast and simple method of producing a sequence of consistent—but rounded—bends.

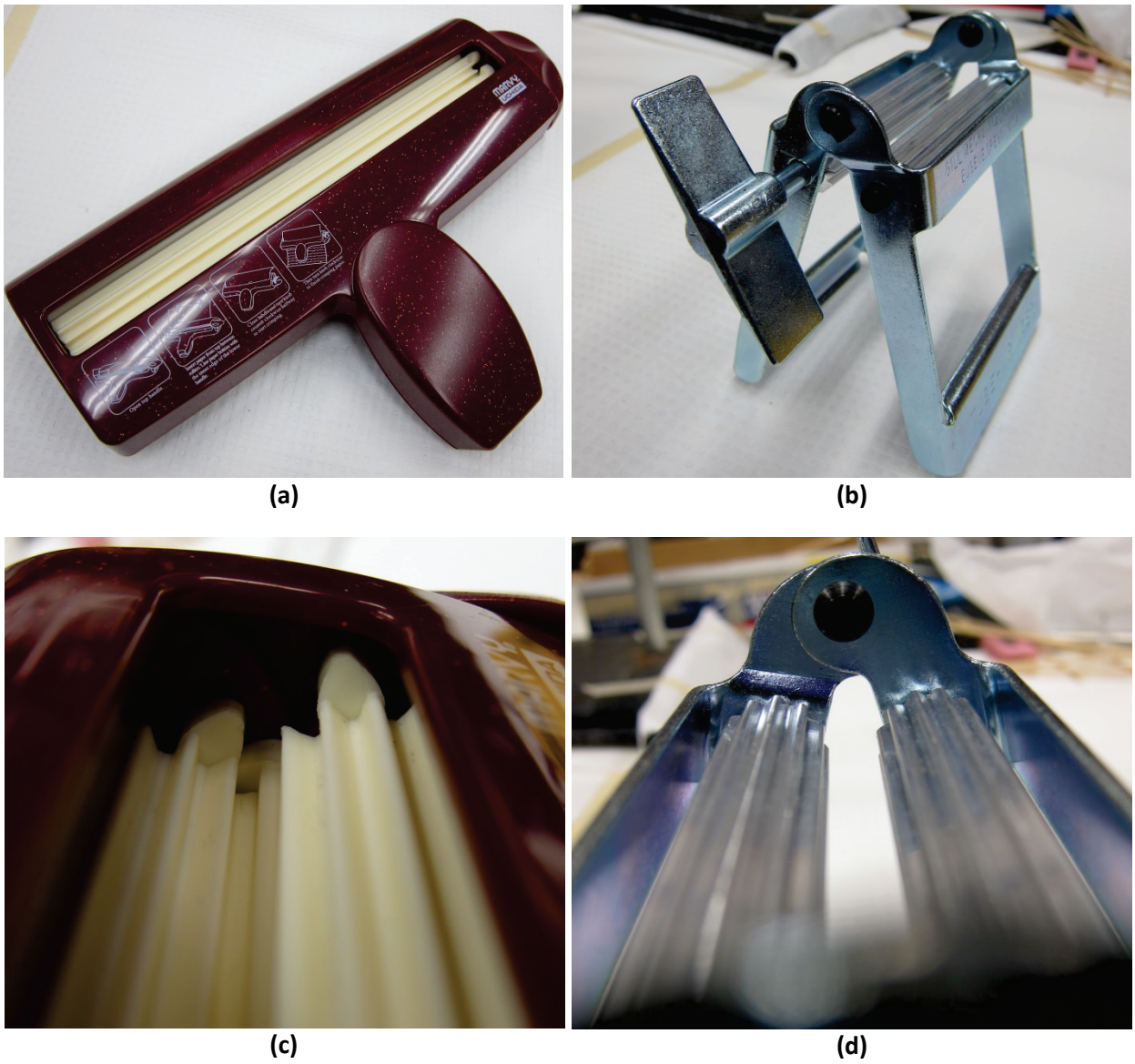

ESM Figure A-12. We tested two corrugator-like tools with different gear tooth profiles: a paper corrugator (panel *a*) with sharp and narrow gear teeth (panel *c*), and a paint-tube wringer (panel *b*) with short and blunt gear teeth (panel *d*).